

# Coherent X-rays reveal anomalous molecular diffusion and cage effects in crowded protein solutions

Anita Girelli<sup>1,2,\*</sup>, Maddalena Bin<sup>1</sup>, Mariia Filianina<sup>1</sup>, Michelle Dargasz<sup>3</sup>, Nimmi Das Anthuparambil<sup>3</sup>, Johannes Möller<sup>4</sup>, Alexey Zozulya<sup>4</sup>, Iason Andronis<sup>1</sup>, Sonja Timmermann<sup>3</sup>, Sharon Berkowicz<sup>1</sup>, Sebastian Retzbach<sup>2</sup>, Mario Reiser<sup>1</sup>, Agha Mohammad Raza<sup>3</sup>, Marvin Kowalski<sup>3</sup>, Mohammad Sayed Akhundzadeh<sup>3</sup>, Jenny Schrage<sup>3</sup>, Chang Hee Woo<sup>10</sup>, Maximilian D. Senft<sup>2</sup>, Lara Franziska Reichart<sup>2</sup>, Aliaksandr Leonau<sup>3</sup>, Prince Prabhu Rajaiah<sup>5,6</sup>, William Chèvremont<sup>7</sup>, Tilo Seydel<sup>8</sup>, Jörg Hallmann<sup>4</sup>, Angel Rodriguez-Fernandez<sup>4</sup>, Jan-Etienne Pudell<sup>4</sup>, Felix Brausse<sup>4</sup>, Ulrike Boesenberg<sup>4</sup>, James Wrigley<sup>4</sup>, Mohamed Youssef<sup>4</sup>, Wei Lu<sup>4</sup>, Wonhyuk Jo<sup>4</sup>, Roman Shayduk<sup>4</sup>, Anders Madsen<sup>4</sup>, Felix Lehmkuhler<sup>5,9</sup>, Michael Paulus<sup>10</sup>, Fajun Zhang<sup>2</sup>, Frank Schreiber<sup>2</sup>, Christian Gutt<sup>3</sup>, and Fivos Perakis<sup>1,\*</sup>

<sup>1</sup>Department of Physics, AlbaNova University Center, Stockholm University, 10691 Stockholm, Sweden

<sup>2</sup>Institut für Angewandte Physik, Universität Tübingen, Auf der Morgenstelle 10, 72076 Tübingen, Germany

<sup>3</sup>Department Physik, Universität Siegen, Walter-Flex-Strasse 3, 57072 Siegen, Germany

<sup>4</sup>European X-Ray Free-Electron Laser Facility, Holzkoppel 4, 22869 Schenefeld, Germany

<sup>5</sup>The Hamburg Centre for Ultrafast Imaging, Luruper Chaussee 149, 22761 Hamburg, Germany

<sup>6</sup>Institute for Biochemistry and Molecular Biology, Laboratory for Structural Biology of Infection and Inflammation, University of Hamburg, c/o DESY, 22603, Hamburg, Germany

<sup>7</sup>ESRF - The European Synchrotron, 71 Avenue des Martyrs, 38042 Grenoble, France

<sup>8</sup>Institut Laue-Langevin, 71 Avenue des Martyrs, 38042 Grenoble, France

<sup>9</sup>Deutsches Elektronen-Synchrotron DESY, Notkestr. 85, 22607 Hamburg, Germany

<sup>10</sup>Fakultät Physik/DELTA, TU Dortmund, 44221 Dortmund, Germany

\*Email: anita.girelli@fysik.su.se, f.perakis@fysik.su.se

## Abstract

Understanding protein motion within the cell is crucial for predicting reaction rates and macromolecular transport in the cytoplasm. A key question is how crowded environments affect protein dynamics through hydrodynamic and direct interactions at molecular length scales. Using megahertz X-ray Photon Correlation Spectroscopy (MHz-XPCS) at the European X-ray Free Electron Laser (EuXFEL), we investigate ferritin diffusion at microsecond time scales. Our results reveal anomalous diffusion, indicated by the non-exponential decay of the intensity autocorrelation function  $g_2(q, t)$  at high concentrations. This behavior is consistent with the presence of cage-trapping in between the short- and long-time protein diffusion regimes. Modeling with the  $\delta\gamma$ -theory of hydrodynamically interacting colloidal spheres successfully reproduces the experimental data by including a scaling factor linked to the protein direct interactions. These findings offer new insights into the complex molecular motion in crowded protein solutions, with potential applications for optimizing ferritin-based drug delivery, where protein diffusion is the rate-limiting step.

## Introduction

In living organisms, proteins are embedded in crowded environments such as in the cytoplasm of cells, membranes, and lipid vesicles [1]. Understanding protein diffusion in these environments is essential, as it directly impacts several critical cellular processes, including metabolism (connected to reaction rates), self-assembly of supramolecular structures and signal transduction [1, 2].

However, predicting and studying protein diffusion in crowded conditions is challenging due to the complex interplay of multiple factors. One such factor is the hydrodynamic interactions, where the motion of each biomolecule is influenced by the flow field generated by its neighbors [3, 4]. These hydrodynamic flows can affect the entire biomembrane and enhance the diffusive motion of passive particles within the cytoplasm [5]. Additionally, protein diffusion is affected by direct forces, including electrostatic interactions and nonspecific attractive interactions between molecules such as van der Waals forces [6]. Excluded volume effects can further complicate diffusion by reducing macromolecular mobility, although these effects alone do not fully account for the tenfold decrease in diffusion rates observed *in vivo* [7, 8]. Moreover, transient protein clusters due to attractive forces can further diminish mobility [6, 9]. A major challenge in understanding protein diffusion in crowded environments lies in deciphering the competition among these factors, all of which influence dynamics on similar time scales.

Crowding can also lead to deviations from simple Brownian motion, which is termed as anomalous diffusion [10, 11]. For globular proteins and colloids, anomalous diffusion has been linked to cage effects [12, 13], where a protein is transiently confined in a "cage" formed by neighboring molecules. The rearrangement of this cage is what eventually allows the molecule to diffuse and leads to structural relaxation. In this context, protein motion is typically characterised in terms of short- and long-time diffusion (see Fig. 1a). Short-time diffusion refers to the motion of the proteins within the cage formed by its neighbors and occurs on time scales shorter than the interaction time  $\tau_i$ , which is the travel time needed for a protein to move a distance equal to its radius. The interaction time can be estimated as  $\tau_i \simeq \frac{R_h^2}{6D_s}$ , where  $R_h$  is the hydrodynamic radius of the protein and  $D_s$  is the average self-diffusion coefficient.

Anomalous diffusion of globular proteins is most evident around the interaction time,  $t \sim \tau_i$  [3]. At time scales much shorter than  $\tau_i$  ( $t \ll \tau_i$ ), the short-time diffusion is Brownian and is mainly affected by hydrodynamic interactions and excluded volume effects [14]. At much longer times ( $t \gg \tau_i$ ), long-time diffusion is predominantly hindered by friction caused by interaction between the proteins [14]. Unlike the short-time diffusion, there are no theoretical predictions for the long-time diffusion due to complex interplay of hydrodynamic and direct protein interactions. Therefore, it is essential to develop strategies to characterize the properties of the long-time diffusion, as well as the transition between the short- and long-time diffusion

regimes.

To understand the role of hydrodynamic and direct interactions in long-time protein motion, it is necessary to measure the collective diffusion at length scales both larger and smaller than the protein intermolecular distances, which is a significant technical challenge. Single particle tracking, fluorescence correlation spectroscopy [15], neutron backscattering, nuclear magnetic resonance (NMR) and gradient field NMR are limited to accessing the self-diffusion of proteins. While scattering techniques can probe collective diffusion, dynamic light scattering (DLS) [16, 17] provides insights at length scales significantly larger than the protein size, while neutron spin echo reflects the short-time diffusion dynamics, typically faster than  $\approx 300$  ns [18–21]. Thus, alongside the theoretical challenges of describing long-time diffusion due to the complexity of interparticle hydrodynamics and direct protein interaction, there is also an experimental research gap. Addressing this gap requires methods that can combine molecular-scale sensitivity with the capability to probe collective dynamics on microsecond time scales.

With the advent of high repetition rate X-ray Free Electron Lasers (XFELs), such as the European XFEL (EuXFEL), it becomes possible to bridge this methodological gap. This capability is especially relevant for biological systems, enabling the study of relatively small proteins (on the order of a several nanometers) at high volume fraction exceeding 20 vol%, which has been previously inaccessible. Measuring dynamics in the microsecond range opens the possibility to probe proteins around the interaction time  $\tau_i$  (estimated in the order of few microseconds) and beyond. X-ray Photon Correlation Spectroscopy (XPCS) enables direct access to collective protein diffusion on molecular length scales [22, 23]. XPCS measurements have been demonstrated for measuring protein dynamics, both indirectly with micro-rheology [24], and directly when related to Brownian diffusion [25], cage relaxation [26, 27], liquid-liquid phase separation dynamics [28–30], gelation processes [31–33], and nanoscale fluctuations in hydration water [34]. The recent development of Megahertz XPCS (MHz-XPCS) at the EuXFEL has further enhanced the ability to capture equilibrium protein diffusion before the onset of radiation effects using the “correlation before aggregation” approach [35]. This technique offers a powerful tool to address the experimental research gap, enabling detailed investigation of long-time protein diffusion at the molecular scale and microsecond time scales, which we exploit in the present study.

Here, we investigate the short- and long-time molecular diffusion and cage effects in crowded protein solutions using MHz-XPCS at the EuXFEL (see Fig. 1b). The central questions are (i) how does the interplay between the hydrodynamic interactions and the direct interactions influence the long-time protein diffusion, (ii) how does the long-time protein diffusion depend on the momentum-transfer  $q$  approaching protein molecular length scales, (iii) what are the characteristic signatures and time and length scales associated with the

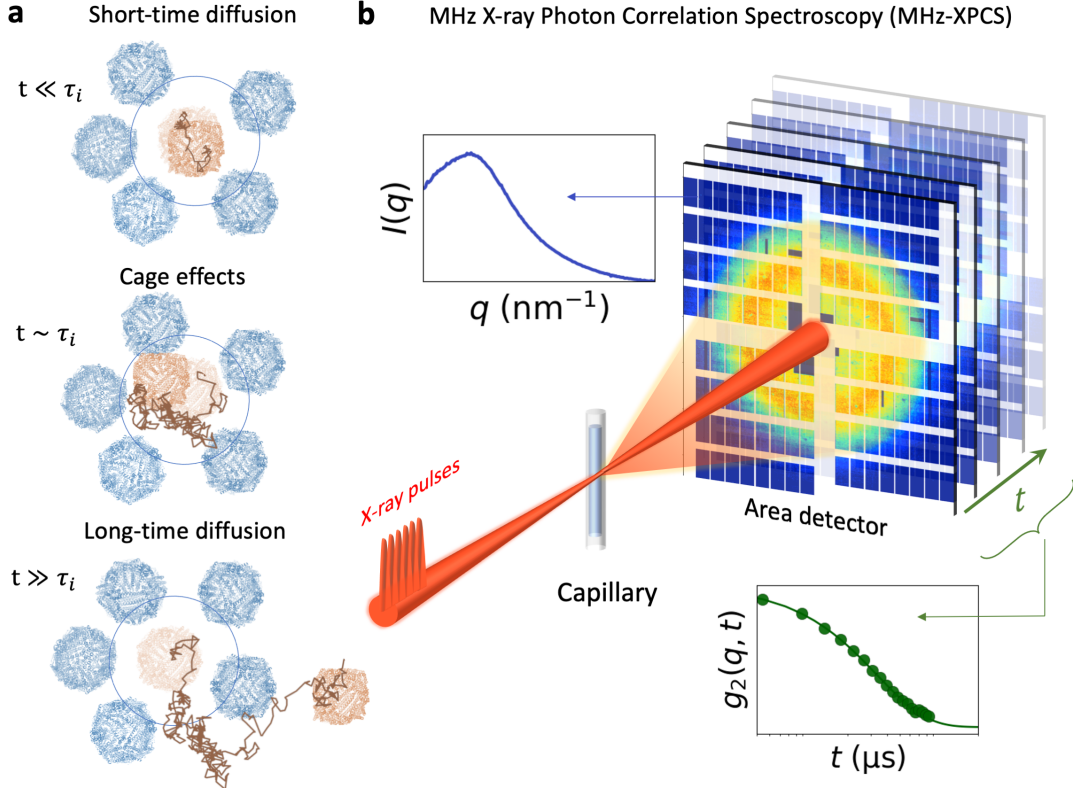


**Fig. 1 | Capturing protein diffusion across different length scales and time scales with MHz-XPCS.** (a) Conceptual representation of ferritin protein molecular dynamics at different time scales. The panels depict the short-time diffusion (top), cage effects (middle) and long-time diffusion (bottom). These different regimes are characterised by the interaction time,  $\tau_i = R_h^2 / (6D_s)$ , where  $R_h$  is the hydrodynamic radius and  $D_s$  the self-diffusion coefficient. (b) Schematic of the Megahertz X-ray Photon Correlation Spectroscopy (MHz-XPCS) experiment. Incident X-ray pulses are scattered from the ferritin protein solutions contained in a capillary. The scattered photons are detected per-pulse with an area detector (AGIPD 1M), capable of recording frames at MHz rate. The scattering intensity as a function of momentum transfer,  $I(q)$ , is obtained by azimuthal integration, while the intensity autocorrelation function  $g_2(q, t)$  is determined by correlating the intensity across frames over time.

cage effects.

To address these questions, we utilize ferritin, a globular protein known for its non-toxic iron-storing capabilities, which is produced by nearly all living organisms. Ferritin has relevant applications in vaccine development [36, 37], drug delivery [38] and nanomaterials [39, 40]. Structurally, ferritin consists of a protein shell with 24 sub-units arranged in pairs to form a hollow nanocage, with a core enriched in iron ions. This robust and monodisperse system is ideal for dynamic measurements, providing strong scattering signal due to the iron-rich core, which facilitates data interpretation. The expected interaction time  $\tau_i$  for ferritin in water is  $\tau_i \approx 0.3 \mu\text{s}$  and  $\tau_i \approx 3 \mu\text{s}$  for ferritin in water-glycerol (with volume fraction  $\nu_{\text{glyc}} = 0.55$ ), calculated using the dilute limit diffusion coefficient as an approximation of  $D_s$  and the experimental  $R_h$  (see Methods).

Our experimental results indicate that as the protein concentration increases, there is a continuous transi-

tion from simple Brownian motion to anomalous diffusion. This transition is characterized by the deviation from single-exponential behavior in the intermediate scattering function, particularly evident at high protein concentrations, where two distinct decay processes become apparent. The hydrodynamic function,  $H(q)$ , is determined experimentally and serves as a signature of many-body hydrodynamic and direct protein interactions. Modeling based on the  $\delta\gamma$ -theory of hydrodynamically interacting colloidal spheres in the short-time limit [41–43] shows quantitative agreement with the experimental results only by accounting for both short- and long-time diffusion.

## Results

### Scattering intensity $I(q)$ and structure factor $S(q)$

The experiments were conducted at the Material Imaging and Dynamics (MID) instrument of the EuXFEL [44], where the protein solutions, contained in capillaries, were measured using a small-angle X-ray scattering (SAXS) geometry with photon energy 10 keV (see Methods). Figure 2a shows the azimuthally integrated intensity,  $I(q)$ , for various protein concentrations, ranging from  $c = 9$  mg/ml (volume fraction  $\phi = 0.0042$ ) to  $c = 730$  mg/ml ( $\phi = 0.34$ ). A spherical form factor fit to the scattering intensity of the dilute solution ( $c = 9$  mg/ml) yields a radius  $R_s \approx 4.0$  nm (see also Supplementary Section 1), corresponding to the size of ferritin cavity [45]. This result suggests that the SAXS signal predominantly originates from the protein core, which exhibits a higher scattering cross-section at this photon energy compared to the protein shell, due to the high iron content.

For the more concentrated solutions ( $c = 70, 180, 400$  and  $730$  mg/ml; see Table 2 for specific sample compositions),  $I(q)$  exhibits correlation peaks that are indicative to the formation of a structure factor  $S(q)$ , as shown in Fig. 2b (see Methods for details on data analysis). The presence of the  $S(q)$  peak at  $q = q_0$  reflects interference between proteins, with a correlation length  $\xi_p = 2\pi/q_0$ . The values of  $q_0$  and  $\xi_p$  are provided in Table 1. As the protein concentration increases, the peak shifts to higher  $q$ -values, indicating that the inter-protein correlation length,  $\xi_p$ , decreases due to crowding. Additionally, Fig. 2b demonstrates that the  $S(q)$  measured at the European Synchrotron Radiation Facility (ESRF), beamline TRUSAXS (ID02), is consistent with the  $S(q)$  obtained at the EuXFEL.

### Intensity autocorrelation functions $g_2(q, t)$ and $q$ -dependent diffusion coefficient $D(q)$

The intensity autocorrelation function,  $g_2(q, t)$ , is shown in Fig. 3a-d (see Methods for definition). The  $g_2(q, t)$  was collected for varying concentrations ( $c = 70, 180, 400$  and  $730$  mg/ml) and  $q$ -values ( $q = 0.225 -$

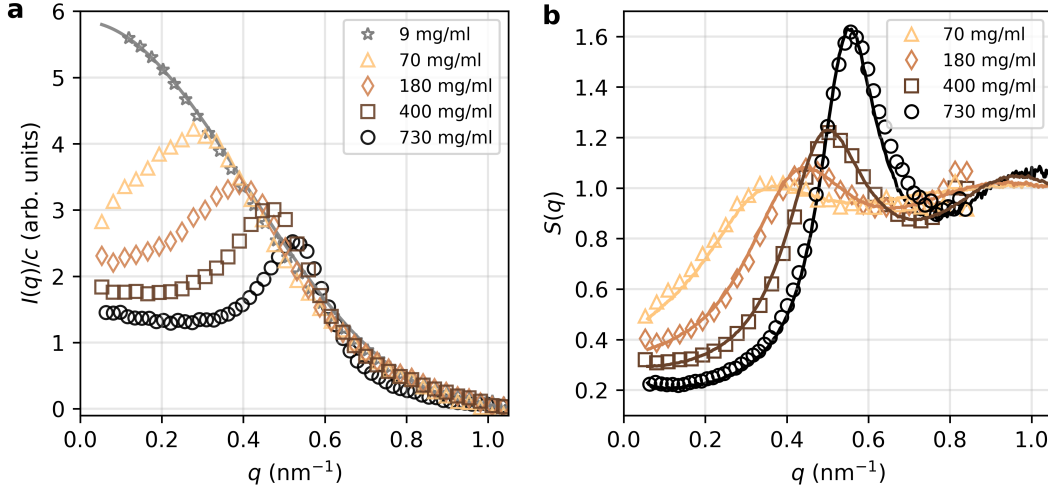


**Fig. 2 | Small-angle X-ray scattering (SAXS) of ferritin solutions.** (a) Scattering intensity as a function of momentum transfer,  $I(q)$ , for different protein concentrations ( $c = 9$  mg/ml to  $c = 730$  mg/ml) obtained at the European XFEL (EuXFEL). The  $I(q)$  curves are background-subtracted and normalized by the respective concentration  $c$ . The solid line represents the spherical form factor fit to the  $I(q)$  data of the dilute solution ( $c = 9$  mg/ml), corresponding to the ferritin cavity with radius  $R_s = 4.0$  nm. (b) The structure factor as a function of momentum transfer,  $S(q)$ , obtained from the experimental data collected at the EuXFEL (empty symbols) shows excellent agreement with the  $S(q)$  obtained at the European Synchrotron Radiation Facility (ESRF, solid lines).

$0.625 \text{ nm}^{-1}$ ), as indicated by the color-code. The solid lines represent the stretched exponential fits according to the equation

$$g_2(q, t) = 1 + \beta(q) \exp[-2(\tilde{\Gamma}(q)t)^\alpha], \quad (1)$$

where  $\beta(q)$  is the speckle contrast, modelled as in Ref. [35],  $\tilde{\Gamma}(q)$  is the decorrelation rate and  $\alpha$  is the Kohlrausch-Williams-Watts (KWW) exponent [46]. As protein concentration increases, we observe an overall slowdown in dynamics and a systematic change of the  $g_2(q, t)$  lineshape from an almost simple exponential decay ( $\alpha = 1$ ) at  $c = 70$  mg/ml to a stretched exponential decay ( $\alpha < 1$ ) at higher concentrations. The condition  $\alpha < 1$  indicates heterogeneous protein motion at elevated concentrations. To account for the varying KWW exponents, we compute the average decorrelation rate [47]  $\Gamma(q) = \tilde{\Gamma}(q)\alpha/\Gamma_f(1/\alpha)$ , where  $\Gamma_f(x)$  is the  $\Gamma$ -function.

The average decorrelation rate,  $\Gamma(q)$ , is shown in Fig. 4a. The solid lines denote the expected relationship  $\Gamma(q) \propto q^2$  for Brownian diffusion. However, the experimental data deviate from this behavior, as highlighted by the shaded regions. To quantify these deviations, we calculate the  $q$ -dependent diffusion coefficient,  $D(q) = \Gamma(q)/q^2$ , shown in Fig. 4b. The diffusion coefficient  $D(q)$  decreases as a function of  $q$ , reaching a minimum at  $q = q_0^D$ , which coincides with  $q_0$  (see Table 1). This modulation in  $D(q)$  is due to the *De Gennes*

**Table 1 | Peak positions  $q_0$  for various protein concentrations  $c$  and corresponding volume fractions  $\phi$ .** The columns represent the peak positions for the structure factor  $S(q)$  (including the correlation length  $\xi_p = 2\pi/q_0$ ), the minimum in the diffusion coefficient  $D(q)$  ( $q_0^D$ ) and the peak position in the hydrodynamic function  $H(q)$  ( $q_0^H$ ), both estimated from the  $\delta\gamma$  model. The error bars for the peak position estimation are  $0.01 \text{ nm}^{-1}$ , due to the  $q$ -resolution of the modelled data, and the  $q$ -binning of the experimental data.

$c$ (mg/ml)	$\phi$	$S(q)$	$D(q)$	$H(q)$
70	0.03	$q_0 = 0.36 \text{ nm}^{-1}$ , $\xi_p = 17.2 \text{ nm}$	$q_0^D = 0.36 \text{ nm}^{-1}$	$q_0^H = 0.38 \text{ nm}^{-1}$
180	0.08	$q_0 = 0.45 \text{ nm}^{-1}$ , $\xi_p = 14.0 \text{ nm}$	$q_0^D = 0.44 \text{ nm}^{-1}$	$q_0^H = 0.45 \text{ nm}^{-1}$
400	0.19	$q_0 = 0.50 \text{ nm}^{-1}$ , $\xi_p = 12.6 \text{ nm}$	$q_0^D = 0.49 \text{ nm}^{-1}$	$q_0^H = 0.49 \text{ nm}^{-1}$
730	0.34	$q_0 = 0.55 \text{ nm}^{-1}$ , $\xi_p = 11.5 \text{ nm}$	$q_0^D = 0.55 \text{ nm}^{-1}$	$q_0^H = 0.55 \text{ nm}^{-1}$

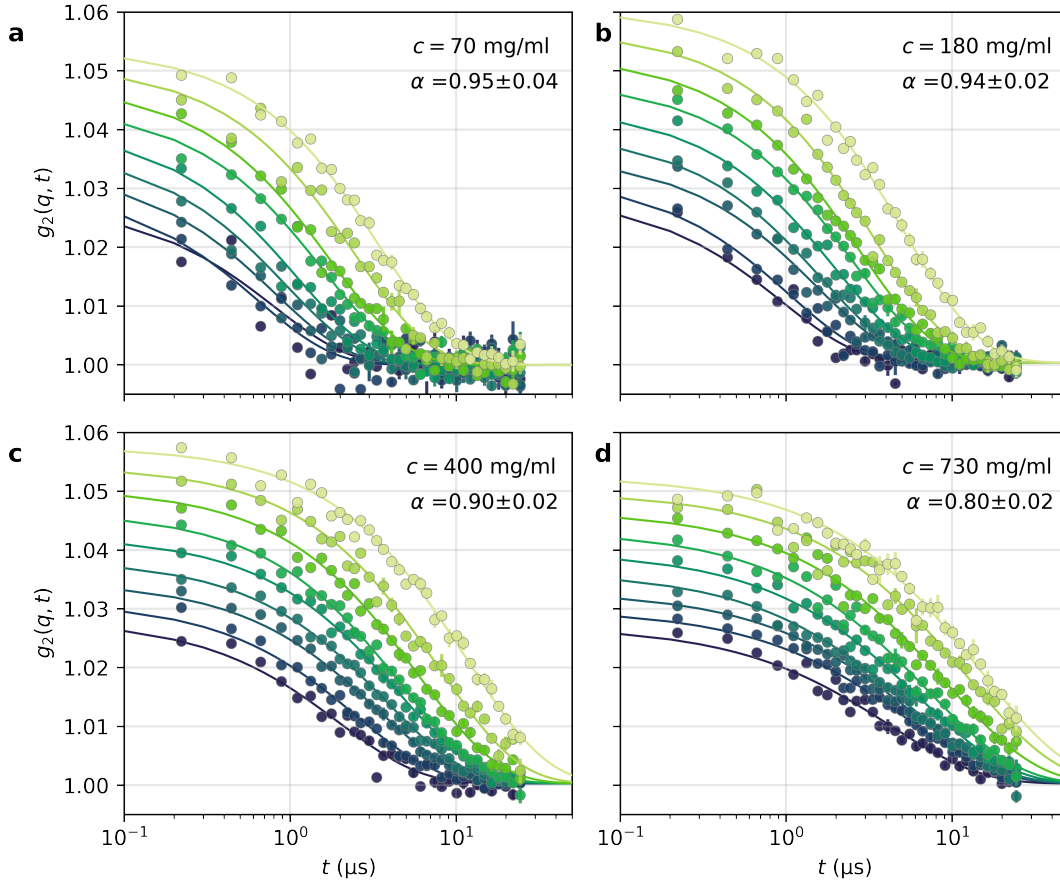


**Fig. 3 | X-ray Photon Correlation Spectroscopy (XPCS) data of ferritin solutions obtained at EuXFEL.** The intensity autocorrelation function,  $g_2(q, t)$ , for different protein concentrations (a)  $c = 70 \text{ mg/ml}$ , (b)  $c = 180 \text{ mg/ml}$ , (c)  $c = 400 \text{ mg/ml}$  and (d)  $c = 730 \text{ mg/ml}$ . Data in panels (a-c) were measured in water-glycerol (with glycerol volume fraction  $\nu_{\text{glyc}} = 0.55$ ), while panel (d) presents data measured in water to reach the desired protein concentration ( $c = 730 \text{ mg/ml}$ ). The different colors represent different  $q$ -values, transitioning from lighter to darker green for  $q$  increasing from  $q = 0.225 \text{ nm}^{-1}$  to  $q = 0.625 \text{ nm}^{-1}$  with equal spacing of  $dq = 0.05 \text{ nm}^{-1}$ . Solid lines represent stretched exponential fits, with the corresponding Kohlrausch-Williams-Watts (KWW) exponent  $\alpha$  shown in the legend.

narrowing [48], observed in a variety of systems [49–54], including apoferritin [19, 55, 56]. Thus, the observed  $D(q)$  indicates that collective protein motion is hindered (i.e. slowed down) by the neighbouring proteins, at

length scales approaching the correlation length  $\xi_p = 2\pi/q_0$ .

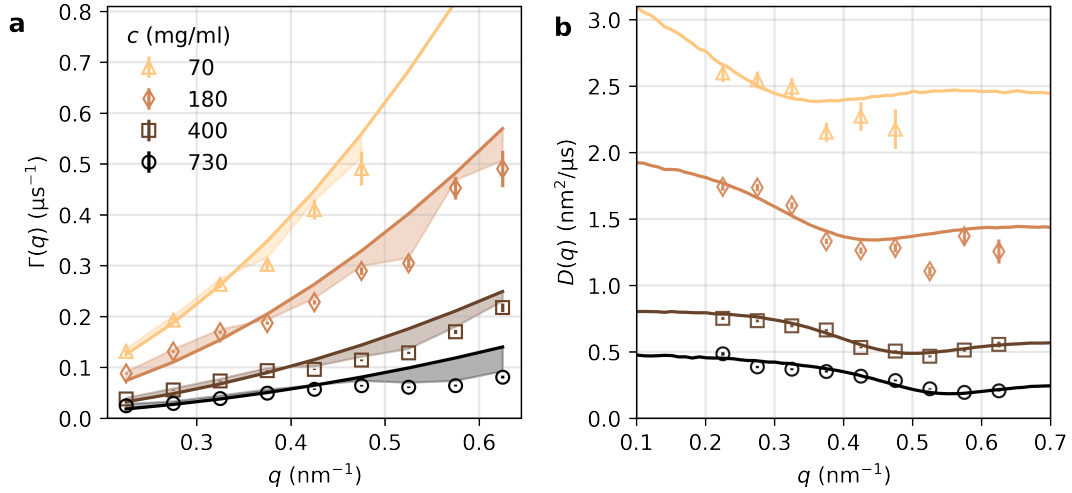


**Fig. 4 | Decorrelation rate  $\Gamma(q)$  and diffusion coefficient  $D(q)$  at different protein concentrations.** (a) Decorrelation rate  $\Gamma(q)$  as a function of momentum transfer  $q$ . Solid lines represent fits with  $\Gamma(q) = Dq^2$ , while shaded areas highlight deviations of the experimental values from the fit. (b) Diffusion coefficient  $D(q) = \Gamma(q)/q^2$  as a function of momentum transfer  $q$ . Solid lines are model fits using  $\delta\gamma$ -theory. The error bars are estimated from the stretched exponential fit including standard error propagation.

### Hydrodynamic function $H(q)$ and self-diffusion coefficient $D_s$

In the short-time limit, the diffusion coefficient  $D(q)$  can be linked to the hydrodynamic interactions by computing the hydrodynamic function  $H(q)$  [14], defined as:

$$H(q) = \frac{D(q)}{D_0} S(q), \quad (2)$$

where  $D_0$  is the diffusion coefficient in the dilute limit and  $S(q)$  the structure factor. Since there is no theoretical description beyond the short-time limit, we use Eq. 2 to estimate the hydrodynamic function, even though the time scale probed exceeds the interaction time and thus can be influenced also by long-time diffusion.

The hydrodynamic function  $H(q)$  can be expressed as a sum of two contributions via [42]

$$H(q) = \tilde{H}(q) + H_0, \quad (3)$$

where  $\tilde{H}(q)$  is the  $q$ -dependent term determined by protein-protein hydrodynamic interactions and the spatial arrangement of the proteins in the solution, i.e. the  $S(q)$ , while  $H_0$  is a  $q$ -independent term, related to the protein self-diffusion  $D_s$  by  $H_0 = D_s/D_0$ . At length scales much smaller than the typical protein-protein correlation length ( $q \gg q_0$ ), the contribution from  $\tilde{H}(q)$  is negligible and thus  $H(q \gg q_0) = D_s/D_0$ .

Figure 5a shows the experimental  $H(q)$  for different ferritin concentrations ( $c = 70, 180, 400$  and  $730$  mg/ml) using Eq. 2. Here,  $S(q)$  was determined from the SAXS data (shown in Fig. 2b) and  $D_0$  from the DLS data (see Methods and Supplementary section 3). The value of  $D_0$  was corrected to account for the beam heating effect (approximately  $\Delta T \approx 1$  K as detailed in Table S1). The hydrodynamic function  $H(q)$  exhibits maxima at  $q = q_0^H$  in agreement with the  $q_0$  values listed in Table 1. At increased protein concentrations, the overall magnitude of  $H(q)$  decreases due to the reduction in the self-diffusion  $D_s$  and enhanced hydrodynamic interactions.

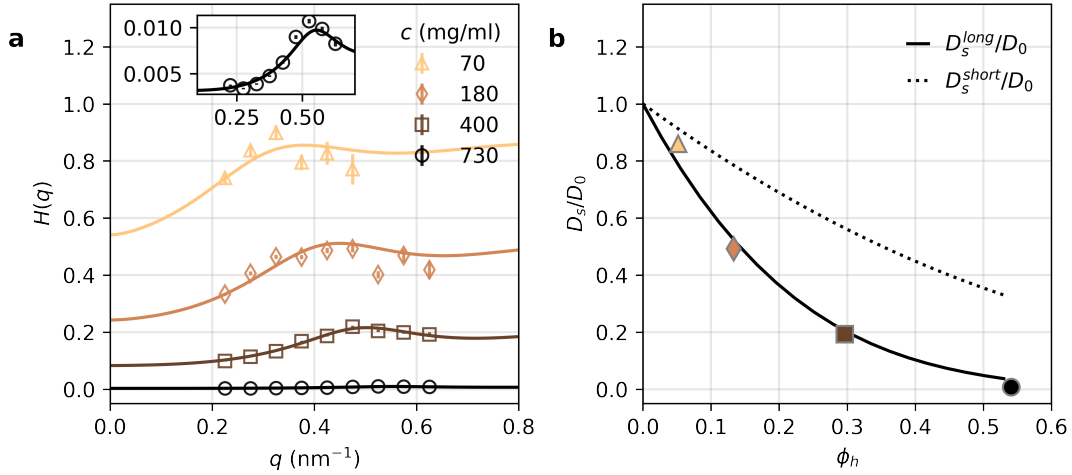


**Fig. 5 | Hydrodynamic function  $H(q)$  and self-diffusion coefficient  $D_s$  for different concentrations.** (a) The experimental  $H(q)$  as a function of momentum transfer  $q$  (empty symbols) and model results using the  $\delta\gamma$ -theory (solid lines). In the inset is shown a zoom in for  $c = 730$  mg/ml. (b) The ratio of the self-over the dilute-limit diffusion coefficients,  $D_s/D_0$ , as a function of the hydrodynamic volume fraction  $\phi_h = \phi \frac{R_h^3}{R_p^3}$ . The lines represent the expected volume fraction dependence of the short-time self-diffusion coefficient  $D_s^{short}/D_0$  [41] (dotted line) and the long-time self-diffusion coefficient  $D_s^{long}/D_0$  [57] (solid line).

### Modelling based on the $\delta\gamma$ -theory

The hydrodynamic function  $H(q)$  was modelled using the colloid  $\delta\gamma$ -theory [14, 41, 42, 58]. This theory accounts for many-body hydrodynamic interactions of spherical particles in suspension in the short-time limit and uses  $S(q)$  as input, as described in the Methods section. Figure 5a shows the model results (solid lines), including a scaling factor that was fitted to the experimental data (see Supplementary Section 5). The model demonstrates good agreement with the experimental values within the measured  $q$ -range. The extracted  $D_s/D_0$  as a function of the hydrodynamic volume fraction is shown in Fig. 5b. The hydrodynamic volume fraction is  $\phi_h = \phi R_h^3/R_p^3 \approx 1.59\phi$ , where  $R_h$  is the protein hydrodynamic radius ( $R_h = 7.25$  nm obtained by DLS, see Methods) and  $R_p$  the protein radius ( $R_p = 6.25$  nm based on the structure reported in Ref [59]).

Alternatively, the hydrodynamic volume fraction  $\phi_h$  dependence of  $D_s/D_0$  can be modeled independently [60]

by the expression

$$D_s^{short}(\phi_h)/D_0 = 1 - 1.73\phi_h + 0.88\phi_h^2, \quad (4)$$

as shown in Fig. 5b (dashed line). This formula, which assumes that  $D_s$  refers to the short-time self-diffusion, appears to overestimate  $D_s/D_0$  in comparison to the experimental values extracted by fitting  $H(q)$ . Such deviations from colloid theory has been observed for various protein systems, including myoglobin [18], hemoglobin [20], and  $\gamma_B$  crystalline [21]. In the case of hemoglobin [20], this discrepancy was partially explained by accounting for the hydrodynamic volume fraction,  $\phi_h = \phi R_h^3/R_p^3 \approx 1.59\phi$ . Here, implementing the  $\phi_h$  correction is insufficient to explain the discrepancy seen for ferritin, where the  $\phi_h$  is included in Fig. 5. Another possible explanation for an overestimation of the  $D_s$  by the theory is the presence of patchy interactions (non-isotropic protein specific interactions) [21], which is presumably *not* the case for ferritin given the repulsive interactions visible in the  $S(q)$  lineshape, characterized by the reduction in the  $S(q=0)$  with increasing concentration, and the presence of a strong correlation peak [16, 17, 61].

At the observed time scales, it is possible that  $D_s/D_0$  is influenced by a combination of short- and long-time diffusion as observed previously by fluorescence recovery after photobleaching (FRAP) experiments [57, 62]. To explore this hypothesis, the long-time self-diffusion coefficient is approximated by [62, 63]

$$D_s^{long} = \frac{D_s^{short}}{D_0} \cdot D_s^{direct} \quad (5)$$

The short-time self-diffusion coefficient,  $D_s^{short}$ , contains the hydrodynamic interactions, but not the direct protein interactions (i.e. electrostatic and nonspecific attractive interactions). The latter are included in  $D_s^{direct} = D_0/(1 + 2\phi_h\chi)$  [64], where  $\chi$  is the contact value of the pair-correlation function, which was estimated approximating the protein interactions as hard spheres (where  $\chi = (1 + 0.5\phi_h)/(1 - \phi_h)^2$ ). This model appears to better describe the volume fraction dependence of the  $D_s/D_0$ , as shown in Fig. 5b (solid line). Therefore, the experimental data indicate that the steep decline of  $D_s/D_0$  with increasing  $\phi_h$  is likely due to the  $D_s^{long}$  component, which becomes dominant with increasing volume fraction.

### Cage effects and long-time diffusion

To investigate the origin of the heterogeneous dynamics indicated by  $\alpha < 1$  for high protein concentrations, we calculate the intermediate scattering function,  $f(q, t)$ , related to the  $g_2(q, t)$  by the Siegert relation,

$$g_2(q, t) = \beta(q)|f(q, t)|^2 + 1. \quad (6)$$

For Brownian diffusion, the  $f(q, t)$  is expected to be a simple exponential function, meaning that  $\ln[f(q, t)]$  depends linearly on time. Figure 6a shows  $f(q, t)$  for different protein concentrations, where the dotted line corresponds to a linear fit over the first 5  $\mu\text{s}$ . We observe that for  $c = 70$  mg/ml, the data follow closely the single exponential fit, while deviations from single exponential behavior become apparent at higher concentrations. Notably, at  $c = 730$  mg/ml, a distinct slope is observed at time scales longer than 5  $\mu\text{s}$ . This deviation is evident for all measured  $q$  values, as shown in Fig. 6b, and becomes more pronounced when  $\ln[f(q, t)]$  is normalized by the slope of the linear fit over the first 5  $\mu\text{s}$ , as seen in Fig. 6d. This observation suggests the presence of two components in the decay.

Using a double exponential fit, we extract the diffusion coefficients of the two components, by:

$$g_2(q, t) = 1 + \beta(q) \{ [1 - A(q)] \exp[-\Gamma_1(q)t] + A(q) \exp[-\Gamma_2(q)t] \}^2, \quad (7)$$

where  $\Gamma_1(q)$  and  $\Gamma_2(q)$  correspond to fast and slow decorrelation rates and  $A(q)$  represents the relative amplitude of the slow component. Figure 6c shows the diffusion coefficients,  $D_1(q) = \Gamma_1(q)/q^2$  and  $D_2(q) = \Gamma_2(q)/q^2$ , obtained from the decorrelation rates of the double exponential fit.  $D_1(q)$  and  $D_2(q)$  exhibit similar  $q$ -dependence and minima for  $q = q_0$  in agreement with the behavior of the  $D(q)$  at lower concentrations, shown in Fig. 4. At  $c = 730$  mg/ml, the ratio  $D_2(q)/D_1(q)$  is  $0.12 \pm 0.04$ .

One possibility is that the slow component is due to aggregates with size  $\approx 8.6$  times larger than a single protein (based on  $D_1(q)/D_2(q)$ ), predicting a correlation peak at  $q = q_0/8.6 = 0.064$  nm $^{-1}$ . However, in the  $S(q)$  data (Fig.2b) we do not see any enhancement at low  $q$ , which would indicate such a peak. Alternatively, the two decays represent short- and long-time diffusion. From  $D_1(q)$ , we estimate  $D_s = D_1(q \rightarrow \infty) = 2.09$  nm $^2$   $\mu\text{s}^{-1}$  which yields an interaction time of  $\tau_i = R_h^2/(6D_s^{short}) = 4.25$   $\mu\text{s}$ . This value corresponds to the cross-over time between the two exponential functions, supporting the hypothesis that the double exponential decay arises from short- and long-time diffusion. It is noteworthy, that estimating the interaction time based on the Stokes-Einstein equation in the dilute limit for ferritin in water yields  $\tau_i \approx 0.3$   $\mu\text{s}$ , whereas in crowded conditions  $\tau_i$  is  $\approx 14.2$  times larger. This calculation implies a significantly slower reaction rates than those predicted from simple Stokes-Einstein estimations, even at molecular length scales.

The lineshape of  $D_1(q)$  and  $D_2(q)$  coincides with the prediction from the  $\delta\gamma$ -theory, as shown in Fig. 6c (black line). Since hydrodynamic forces influence both diffusion coefficients, while direct interactions are relevant only in the long-time diffusion, we conclude that hydrodynamic forces act similarly on the short- and long-time diffusion and the direct interactions do not provide additional  $q$ -dependent changes on the diffusion coefficient. These results are also in agreement with studies performed on larger colloidal particles [65–

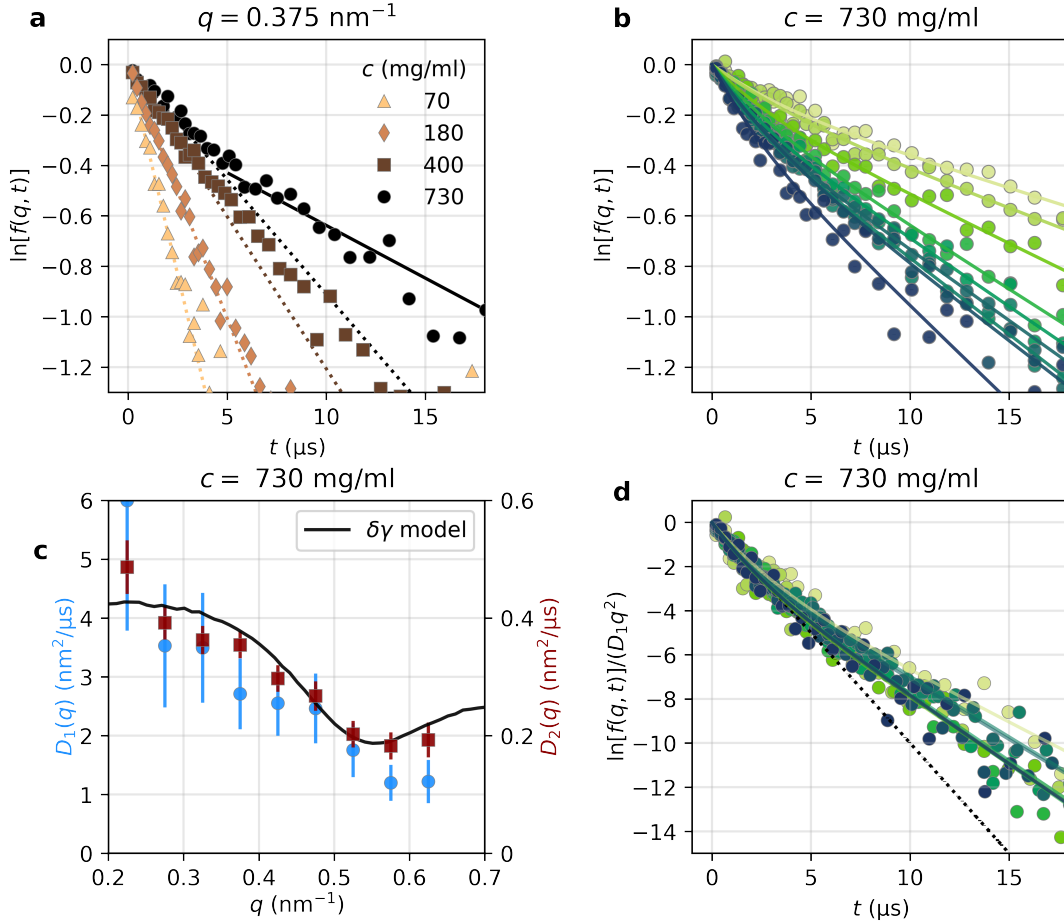


**Fig. 6 | Evidence of short- and long-time diffusion.** (a) The intermediate scattering function  $f(q, t)$  as a function of time (shown in  $\ln[f(q, t)]$ ) at  $q = 0.38 \text{ nm}^{-1}$  for different ferritin concentrations ( $c = 70, 180, 400, 730 \text{ mg/ml}$ ). The dotted lines are linear fits in the time range up to  $5 \mu\text{s}$ . The solid line is a linear fit for time longer than  $5 \mu\text{s}$ . (b) The  $\ln[f(q, t)]$  of ferritin  $c = 730 \text{ mg/ml}$  at  $q$  values from  $q = 0.225 \text{ nm}^{-1}$  to  $q = 0.625 \text{ nm}^{-1}$  from lighter to darker green. (c) The  $q$ -dependent diffusion constants extracted with a double exponential fit. The blue circles are  $D_1(q) = \Gamma_1(q)/q^2$  (left hand side y-axis) and the red squares are  $D_2(q) = \Gamma_2(q)/q^2$  (right hand side y-axis). The solid black line is the modelled  $D(q)$ , from the  $\delta\gamma$  also shown in Fig. 4b and refers to the y axis on the right hand side. (d)  $\ln[f(q, t)]$  normalised by slope of the  $\ln[f(q, t)]$  in the time range up to  $5 \mu\text{s}$ . The dotted line is a linear fit in the time range up to  $5 \mu\text{s}$ .

67], where the short- and long-time diffusion coefficients,  $D^{short}(q)$  and  $D^{long}(q)$ , were shown to have the same lineshape at  $qR > 2.5$ . This finding indicates that for the investigated system at  $1.5 < qR < 4$ , the direct interactions, relevant only for the long-time diffusion, do not influence the  $q$ -dependence of  $D(q)$ . Consequently, hydrodynamic functions can be effectively extracted from long-time diffusion, disentangling the contributions of direct forces and hydrodynamic interactions (see also Supplementary Section 5).

Additionally, the relative amplitude of the two decays,  $A(q)$ , provides insight into protein motion. It is

given by:

$$A(q) = A_0 \exp\left(-\frac{q^2 \delta^2}{6}\right), \quad (8)$$

reflecting the loss of correlation due to an Debye–Waller-like movement around a central position, with average displacement  $\delta$  and percentage  $A_0$  of particles involved [68]. For this system,  $A_0 = 90 \pm 3\%$  and  $\delta = 1.2 \pm 0.6$  nm indicating that the majority of protein molecules participate in cage formation, with an average displacement of 1.2 nm. This finding suggests that protein rattling within the cage occurs only within a fraction of their radius due to the limited available space at high concentrations. This result aligns with the expected reduction in cage size due to confinement with increasing volume fraction, approaching the glass transition [12, 69].

## Discussion

In summary, we present results from MHz-XPCS experiments conducted at the EuXFEL, complemented by modelling based on colloid theory, focusing on concentrated ferritin solutions. A key advantage of this experimental approach is its ability to capture the long-time protein diffusion at length scales comparable to the average protein-protein distance in crowded conditions. In contrast to short-time diffusion, there are no theoretical predictions for long-time diffusion that adequately account for hydrodynamic interactions and direct interactions.

Our results reveal anomalous diffusion in highly concentrated ferritin solutions, which becomes more pronounced with increasing protein concentration. From the momentum-transfer dependent diffusion coefficient,  $D(q)$ , and the corresponding structure factor,  $S(q)$ , we extract the hydrodynamic function  $H(q)$ , which quantifies contributions from many-body hydrodynamic interactions. Modeling based on the  $\delta\gamma$ -theory of hydrodynamically interacting colloidal spheres [41, 42] shows good agreement with the experimental  $H(q)$  when a scaling is applied. Notably, the  $H(q)$  intercept, related to the ratio of the self- over the dilute-limit diffusion coefficients,  $D_s/D_0$ , decreases with volume fraction much more rapidly than expected for purely short-time diffusive motion. This finding indicates that both short- and long-time diffusion contribute to self-diffusion, with the long-time diffusion becoming more significant as the protein concentration increases.

Further evidence for the coexistence of short- and long-time diffusion comes from the analysis of the intensity autocorrelation function,  $g_2(q, t)$ . The  $g_2(q, t)$  exhibits a double exponential decay with increasing protein concentration, which is especially pronounced at the highest concentration,  $c = 730$  mg/ml. The data suggest that the short- and long-time diffusion coefficients,  $D^{short}(q)$  and  $D^{long}(q)$ , exhibit nearly identical  $q$ -dependence differing only by a scaling factor, as previously observed in colloidal suspensions [65]. This finding indicates that long-time diffusion is governed by both hydrodynamic effects and direct inter-

actions. We observe that the latter contribute to an  $q$ -independent decrease of the diffusion coefficient for  $1.5 < qR < 4$ . At the highest concentration ( $c = 730$  mg/ml), cage effects are observed with an average displacement of  $\delta = 1.2 \pm 0.6$  nm, indicating that cage-trapping occurs within a fraction of the protein radius due to confinement. These effects can explain quantitatively the observed anomalous diffusion but also provide a molecular mechanism for the reduced mobility of proteins under crowded conditions.

From a broader perspective, our findings can facilitate biomedical applications involving ferritin as a nano-drug delivery system [38] and nano-reactor [70], as in sustained-release preparations the accurate determination of the anomalous diffusion coefficients can significantly influence the bioavailability profile. Future work that builds on the results presented here has the potential to focus on environments more closely resembling biological conditions, by introducing crowders of different sizes (e.g., polymers, proteins, polysaccharides) in order to explore the effects of polydispersity on long-time diffusion [71].

## Methods

### Sample Preparation

Protein solutions of different concentrations were prepared in steps, starting from centrifuging the parent protein saline solution and followed by dilution with glycerol. Ferritin from equine spleen solutions (Sigma-Aldrich, F4503) was used as the parent solution, with an initial protein concentration of  $c = 71$  mg/ml and NaCl content of 150 mM. This parent solution was centrifuged at 10000 g for 1 hour using 10 kDa Millipore filters, resulting in a concentrated ferritin solution of approximately  $c \approx 730$  mg/ml, as determined by UV-Vis spectroscopy at  $\lambda = 280$  nm [72]. This concentration was estimated using a calibration curve based on samples of known concentration.

The concentrated ferritin solution was subsequently diluted with glycerol and water to achieve protein concentrations  $c = 70, 180, 400$  mg/ml (with 55 vol% glycerol). As the protein concentration decreased, the NaCl concentration also decreased, as the diluting solvent did not contain NaCl. These solutions were filled in quartz capillaries with an outer diameter of  $\approx 1$  mm and a wall thickness of  $\approx 20$   $\mu$ m. The volume fraction is calculated from the protein concentration,  $c$ , using the equation  $\phi = c\nu_s$ , where  $\nu_s = 0.465$  ml/g is the specific volume of the protein [73], which is the inverse of the protein density. A summary of the samples and their composition is shown in Table 2.

**Table 2 | Samples composition including protein concentration  $c$ , glycerol volume fraction  $\nu_g$ , and NaCl concentration  $c_s$ .**

$c$ (mg/ml)	$\nu_{\text{glyc}}$	$c_s$ (mM)
70	0.55	15
180	0.55	35
400	0.55	80
730	0	150

### X-ray experimental parameters

The data were acquired at the MID instrument [44] of the EuXFEL in small-angle X-ray scattering (SAXS) configuration using a pink beam with a photon energy of 10 keV. The X-ray pulses, with a intra-train repetition rate of 4.5 MHz (221.5 ns pulse spacing), were delivered in trains of up to 310 pulses, with a inter-train repetition rate of 10 Hz. The Adaptive Gain Integrating Pixel Detector (AGIPD) [74, 75] was positioned at a sample-detector distance of 7.687 m. The X-ray beam was focused to a diameter of  $12 \pm 1 \mu\text{m}$  and the X-ray bandwidth was  $\Delta E/E = 7 \times 10^{-3}$ , determined by fitting the speckle contrast. This beam size, achieved using compound refractive lenses (CRL), was chosen to enhance both the speckle contrast and the signal-to-noise ratio (SNR) of the XPCS measurements [76]. X-ray intensity was adjusted by chemically vapor deposited (CVD) diamond attenuators of variable thickness to minimise beam-induced effects while maintaining high SNR (see Table S1). To refresh the sample volume between trains, the sample was moved through the X-ray beam at a translation motor speed of  $0.4 \text{ mm s}^{-1}$ , as described in Ref. [35]. Table 3 summarises the experimental parameters for the EuXFEL measurements, along with the SAXS experimental parameters at ESRF (beamline ID02).

**Table 3 | The X-ray parameters used at the European XFEL (EuXFEL) and European Synchrotron Radiation Facility (ESRF)**

Parameter	EuXFEL (MID)	ESRF (ID02)
Photon energy (keV)	10.0	12.23
Frame rate	4.5 MHz/10 Hz (intra-/inter-train)	10 Hz
Beam size ( $\mu\text{m}^2$ )	$12 \times 12$	$35 \times 35$
Sample environment	1mm quartz capillaries	1mm quartz capillaries
Detector	AGIPD	EIGER2 4M
Pixel size ( $\mu\text{m}^2$ )	$200 \times 200$	$75 \times 75$
Sample-detector distance (m)	7.687	1.48

### Brownian diffusion coefficient $D_0$ and hydrodynamic radius $R_h$

The protein diffusion coefficient,  $D_0$ , was measured at dilute conditions ( $c = 9 \text{ mg/ml}$ ) using DLS (see Section 4 of Supplementary Information). For ferritin in water-glycerol (55 vol% glycerol), we obtained

$D_0 = 4.28 \pm 0.03 \text{ nm}^2 \mu\text{s}^{-1}$  while for ferritin in water the diffusion coefficient is  $D_0 = 30.1 \pm 0.2 \text{ nm}^2 \mu\text{s}^{-1}$ . The hydrodynamic radius,  $R_h$ , was calculated using the Stokes-Einstein equation,  $D_0 = k_B T / (6\pi\eta R_h)$ , where  $\eta$  is the viscosity,  $T$  the temperature and  $k_B$  the Boltzmann constant. Here, by using  $\eta = 92 \text{ mPa s}$  [77] and  $T = 298 \text{ K}$ , we estimated  $R_h = 7.3 \pm 0.1 \text{ nm}$ . This value is comparable to literature values of apoferritin (hollow shell without the core) in saline solutions obtained with DLS ( $R_h = 6.9 \text{ nm}$  [16],  $R_h = 6.3 \text{ nm}$  [17]) and HYDROPRO ( $R_h = 6.4 \text{ nm}$ ) [78]. The slightly larger  $R_h$  obtained here could be due to the presence of the iron (ferritin vs apoferritin), which may influence the protein hydrodynamic radius as surrounding hydration layer. For ferritin solutions, the  $R_h = 6.85 \pm 0.8 \text{ nm}$  obtained by DLS [79] is consistent with our estimation.

### SAXS data analysis

The protein scattering intensity,  $I(q)$ , was determined by subtracting the background scattering intensity,  $I_{\text{bkg}}$  (scattering from the capillary containing only the solvent), from the measured scattering intensity,  $I_m(q)$ :

$$I(q) = I_m(q) - I_{\text{bkg}}(q). \quad (9)$$

The scattering intensity,  $I(q)$ , of mono-dispersed spherical proteins is modelled by

$$I(q) = c\Delta\rho^2 P(q)S(q), \quad (10)$$

where  $\Delta\rho$  is the scattering contrast between the protein and the solvent,  $c$  the protein concentration,  $S(q)$  the structure factor, and  $P(q)$  the form factor. The  $P(q)$  was determined experimentally by measuring the scattering intensity in the dilute limit,  $I_0(q)$ , where  $S(q) \approx 1$ . Here,  $I_0(q)$  is estimated using low concentration sample ( $c = 9 \text{ mg/ml}$ ). The experimental  $S(q)$  was then calculated as follows:

$$S(q) = C \frac{I_m(q) - I_{\text{bkg}}(q)}{I_0(q) - I_{\text{bkg}}(q)}, \quad (11)$$

where  $C$  is a normalization constant. More detailed are provided in section 1 of the Supplementary Information.

## Intensity autocorrelation function $g_2$ calculation

The  $g_2(q, t)$  function was calculated starting from the two time correlation function (TTCs), which represent the correlation between speckle images taken at times  $t_1$  and  $t_2$  at momentum transfer  $q$ :

$$c_2(q, t_1, t_2) = \frac{\langle I(q, t_1)I(q, t_2) \rangle}{\langle I(q, t_1) \rangle \langle I(q, t_2) \rangle} \quad (12)$$

where  $\langle \dots \rangle$  indicates averaging over all pixels with the same momentum transfer,  $q$ . The  $g_2(q, t)$  functions were analyzed with the MID data processing pipeline embedded to the DAMNIT tool of the EuXFEL data analysis group (<https://damnit.readthedocs.io/en/latest/>) The average TTC was obtained by averaging the TTCs of the single trains, where the weights correspond standard error on the TTCs. The corresponding error bars were estimated from the standard error between the individual TTCs. Finally,  $g_2(t, q)$  was obtained by  $g_2(q, t) = \langle c_2(q, t_1, t_1 + t) \rangle_{t_1}$ .

## Beam-induced effects assessment

Identifying the onset of X-ray beam-induced effects is crucial for MHz-XPCS. Beam-induced effects can manifest as fluence-dependent changes in the scattering intensity,  $I(q)$ , and the diffusion coefficient,  $D(q)$ . These changes may result from beam-induced heating or radicals formation in the solution, potentially leading to protein aggregation or denaturation [35].

Supplementary Fig. S2 shows the  $I(q)$  for varying pulse accumulations at different concentrations,  $c$ , and transmissions,  $T_0$ . In addition, the  $I(q)$  as a function of pulse number for  $q = 0.2 \text{ nm}^{-1}$  is shown in Supplementary Fig. S3. Minor changes in the  $I(q)$  are observed across all  $T_0$ . Specifically for data used for the figures presented, i.e. at  $T_0 = 5.35 \times 10^{-6}$ , intensity changes are less than 1%.

The fluence-dependence of  $D(q)$  and TTCs are discussed in Supplementary Section 3. Within the error bars, changes in the KWW exponent  $\alpha$  with dose are negligible. However, a slight increase in the diffusion coefficient is observed with increasing pulse number, likely due to beam-induced temperature rise [35, 80], estimated to be below 1 K. This approach allows us to identify the optimal parameters to mitigate beam-induced effects, such as optimal transmission  $T_0$ , number of repetitions  $n_{\text{rep}}$ , and the number of pulses-per-train  $n_{\text{pulses}}$ . Considering the minor changes in both  $I(q)$  and  $D(q)$  under these conditions, we conclude that protein aggregation is not detected. The intrinsic protein dynamics can be accurately accessed by including a correction for the temperature increase (in the order of 1 K) as reported in Table S2.

## Hydrodynamic function modelling

The hydrodynamic function,  $H(q)$ , was modelled according to the framework outlined in Ref. [42, 58] by:

$$H(q) = \tilde{H}(q) + \frac{D_s(\phi)}{D_0} \quad (13)$$

The  $q$ -dependent part  $\tilde{H}(q)$  is calculated using *jscatter* [81] with the expression:

$$\tilde{H}(q) = \frac{3}{2\pi} \int_0^\infty dR_p k \frac{\sin^2(R_p k)}{(R_p k)^2 [1 + \phi S_\gamma(R_p k)]} \int_{-1}^1 dx (1 - x^2) [S(|\mathbf{q} - \mathbf{k}|) - 1], \quad (14)$$

where  $x = \cos(\mathbf{q}, \mathbf{k})$  is the angle between  $\mathbf{q}$  and  $\mathbf{k}$  vectors,  $\phi$  is the protein volume fraction. The protein radius  $R_p = 6.25$  nm is based on the structure reported in Ref [59], and  $S_\gamma(q)$  is the volume fraction dependent function given in Ref. [58]. The  $S(q)$  used for the calculation is obtained by interpolating the experimental  $S(q)$  (see Supplementary Section 1).

The normalized self-diffusion coefficient  $\frac{D_s(\phi)}{D_0}$  was estimated via [58]:

$$\frac{D_s(\phi)}{D_0} = \frac{1}{2\pi} \int_0^\infty dR_p k \frac{\sin^2(R_p k)}{(R_p k)^2 [1 + \phi S_\gamma(R_p k)]} \quad (15)$$

More information on the fit is provided in the Supplementary Section 5.

## Acknowledgements

We acknowledge the European XFEL in Schenefeld, Germany, for provision of XFEL beamtime at the Scientific Instrument MID (Materials Imaging and Dynamics) and would like to thank the staff for their assistance. The data presented here are collected as part of measurement time awarded to proposals 3094 and 5397. In addition, we acknowledge Maxwell cluster for providing computer resources to perform the analysis. We thank the European Synchrotron Radiation Facility (ESRF) for provision of synchrotron radiation facilities at TRUSAXS instrument (Time Resolved Ultra Small Angle X-ray Scattering), ID02 (SC-5485) with additional support from Theyencheri Narayanan. FP acknowledges financial support by the Swedish National Research Council (Vetenskapsrådet) under Grant No. 2019-05542, 2023-05339 and within the Röntgen-Ångström Cluster Grant No. 2019-06075, and the kind financial support from Knut och Alice Wallenberg foundation (WAF, Grant. No. 2023.0052). This research is supported by the Center of Molecular Water Science (CMWS) of DESY in an Early Science Project, the MaxWater initiative of the Max-Planck-Gesellschaft (Project No. CTS21:1589), Carl Tryggers and the Wenner-Gren Foundations (Project No. UPD2021-0144). This project has also received funding from the European Union's Horizon 2020 research and innovation programme under the

Marie Skłodowska-Curie grant agreement No. 101081419 (PRISMAS) and 101149230 (CRYSTAL-X). We also acknowledge BMBR ErUM-Pro funding (05K22PS1, CG), BMBF (05K19PS1 and 05K20PSA, CG ; 05K19VTB, FS and FZ), DFG-ANR (SCHR700/28-1, SCHR700/42-1, ANR-21-CE06-0047 IDPXN, FS, FZ, and TS). FL and PPR thank the Cluster of Excellence “Advanced Imaging of Matter” of the Deutsche Forschungsgemeinschaft (DFG)–EXC 2056–project id no. 390715994. AL and CG acknowledge financial support by the consortium DAPHNE4NFDI in association with the German National Research Data Infrastructure (NFDI) e.V. - project number 46024879. MP thanks the DELTA machine group for providing synchrotron radiation for sample characterization.

## **Author contributions**

AG, MR and FP designed the experiment, along with discussions with CG, FS, FZ, MP, JM, TS and FL. AG, MB and MF prepared and handled the samples. JH, AR-F, J-EP, FB, UB, WL, WJ, RS, AZ, JM and AM operated MID and collected data together with the rest of the experimental team. AG, MB, MF, ST and IA performed online data processing and analysis at MID, based on scripts developed by MR and the MID data analysis team (JW and AL being the main contributors). SB, SR, MS, LR, and MD were in addition responsible for the elog. Experiments at ESRF were supported by WC. AG performed offline data processing and analysis with input from FP, FZ, CG and MP. All authors jointly performed the experiments and discussed the final results. The manuscript was written by AG and FP with input from all authors.

## **Competing interests**

The authors declare no competing interests.

## **Data availability**

Data recorded for the experiment at the European XFEL are available at [doi:10.22003/XFEL.EU-DATA-003094-00] and [doi:10.22003/XFEL.EU-DATA-005397-00]. Data recorded at ESRF are available at [doi:10.1515/ESRF-ES-1435809276].

## **Code availability**

The code used to analyse the data in this study is available from the corresponding authors upon request.

## References

1. Dix, J. A. & Verkman, A. S. Crowding Effects on Diffusion in Solutions and Cells. *Annu. Rev. Biophys.* **37**, 247–263 (2008).
2. Zimmerman, S. & Minton, A. Macromolecular crowding: biochemical, biophysical, and physiological consequences. *Annu. Rev. Biophys. Biomol. Struct.* **22**, 27–65 (1993).
3. Grimaldo, M., Roosen-Runge, F., Zhang, F., Schreiber, F. & Seydel, T. Dynamics of proteins in solution. *Q. Rev. Biophys.* **52**, e7 (2019).
4. Maheshwari, A. J., Sunol, A. M., Gonzalez, E., Endy, D. & Zia, R. N. Colloidal hydrodynamics of biological cells: A frontier spanning two fields. *Phys. Rev. Fluids* **4**, 110506 (2019).
5. Mikhailov, A. S. & Kapral, R. Hydrodynamic collective effects of active protein machines in solution and lipid bilayers. *Proc. Natl. Acad. Sci. U.S.A.* **112**, E3639–E3644 (2015).
6. Ando, T. & Skolnick, J. Crowding and hydrodynamic interactions likely dominate in vivo macromolecular motion. *Proc. Natl. Acad. Sci. U.S.A.* **107**, 18457–18462 (2010).
7. Elowitz, M. B., Surette, M. G., Wolf, P.-E., Stock, J. B. & Leibler, S. Protein Mobility in the Cytoplasm of *Escherichia coli*. *J. Bacteriol.* **181**, 197–203 (1999).
8. Konopka, M. C., Shkel, I. A., Cayley, S., Record, M. T. & Weisshaar, J. C. Crowding and Confinement Effects on Protein Diffusion In Vivo. *J. Bacteriol.* **188**, 6115–6123 (2006).
9. Bülow, S. v., Siggel, M., Linke, M. & Hummer, G. Dynamic cluster formation determines viscosity and diffusion in dense protein solutions. *Proc. Natl. Acad. Sci. U.S.A.* **116**, 9843–9852 (2019).
10. Banks, D. S. & Fradin, C. Anomalous Diffusion of Proteins Due to Molecular Crowding. *Biophys. J.* **89**, 2960–2971 (2005).
11. Weiss, M., Elsner, M., Kartberg, F. & Nilsson, T. Anomalous Subdiffusion Is a Measure for Cytoplasmic Crowding in Living Cells. *Biophys. J.* **87**, 3518–3524 (2004).
12. Weeks, E. R. & Weitz, D. A. Properties of Cage Rearrangements Observed near the Colloidal Glass Transition. *Phys. Rev. Lett.* **89**, 095704 (2002).
13. Kegel, W. K., van Blaaderen & Alfons. Direct observation of dynamical heterogeneities in colloidal hard-sphere suspensions. *Science* **287**, 290–293 (2000).
14. Nägele, G. On the dynamics and structure of charge-stabilized suspensions. *Phys. Rep.* **272**, 215–372 (1996).

15. Bacia, K., Kim, S. A. & Schwille, P. Fluorescence cross-correlation spectroscopy in living cells. *Nat. Methods* **3**, 83–89 (2006).
16. Häußler, W., Wilk, A., Gapinski, J. & Patkowski, A. Interparticle correlations due to electrostatic interactions: A small angle X-ray and dynamic light scattering study. I. Apoferritin. *J. Chem. Phys.* **117**, 413 (2002).
17. Petsev, D. N. & Vekilov, P. G. Evidence for Non-DLVO Hydration Interactions in Solutions of the Protein Apoferritin. *Phys. Rev. Lett.* **84**, 1339–1342 (2000).
18. Longeville, S., Doster, W. & Kali, G. Myoglobin in crowded solutions: structure and diffusion. *Chem. Phys.* **292**, 413–424 (2003).
19. Gapinski, J. *et al.* Diffusion and microstructural properties of solutions charged nanosized proteins: experiment versus theory. *J. Chem. Phys.* **123**, 054708 (2005).
20. Doster, W. & Longeville, S. Microscopic Diffusion and Hydrodynamic Interactions of Hemoglobin in Red Blood Cells. *Biophys. J.* **93**, 1360–1368 (2007).
21. Bucciarelli, S. *et al.* Dramatic influence of patchy attractions on short-time protein diffusion under crowded conditions. *Sci. Adv.* **2**, e1601432 (2016).
22. Moeller, J., Sprung, M., Madsen, A. & Gutt, C. X-ray photon correlation spectroscopy of protein dynamics at nearly diffraction-limited storage rings. *J. Synchrotron Radiat.* **6**, 794–803 (2019).
23. Perakis, F. & Gutt, C. Towards molecular movies with X-ray photon correlation spectroscopy. *Phys. Chem. Chem. Phys.* **22**, 19443–19453 (2020).
24. Otto, F. *et al.* The dynamics of PEG-coated nanoparticles in concentrated protein solutions up to the molecular crowding range. *Aggregate* **5**, e483 (2024).
25. Switalski, K. *et al.* Direct measurement of Stokes–Einstein diffusion of Cowpea mosaic virus with 19  $\mu$ s-resolved XPCS. *J. Synchrotron Radiat.* **29**, 1429–1435 (2022).
26. Vodnala, P. *et al.* Hard-sphere-like dynamics in highly concentrated alpha-crystallin suspensions. *Phys. Rev. E* **97**, 020601(R) (2018).
27. Chushkin, Y. *et al.* Probing cage relaxation in concentrated protein solutions by XPCS. *Phys. Rev. Lett.* **129**, 238001 (2022).
28. Girelli, A. *et al.* Microscopic Dynamics of Liquid-Liquid Phase Separation and Domain Coarsening in a Protein Solution Revealed by X-ray Photon Correlation Spectroscopy. *Phys. Rev. Lett.* **126**, 138004 (2021).

29. Moron, M. *et al.* Gelation Dynamics upon Pressure-Induced Liquid–Liquid Phase Separation in a Water–Lysozyme Solution. *J. Phys. Chem. B* **126**, 4160–4167 (2022).
30. Do Amaral, M. J. *et al.* Copper drives prion protein phase separation and modulates aggregation. *Sci. Adv.* **9**, eadi7347 (2023).
31. Begam, N. *et al.* Kinetics of network formation and heterogeneous dynamics of an egg white gel revealed by coherent X-ray scattering. *Phys. Rev. Lett.* **126**, 098001 (2021).
32. Timmermann, S. *et al.* X-ray driven and intrinsic dynamics in protein gels. *Sci. Rep.* **13**, 11048 (2023).
33. Anthuparambil, N. D. *et al.* Exploring non-equilibrium processes and spatio-temporal scaling laws in heated egg yolk using coherent X-rays. *Nat. Commun.* **14**, 5580 (2023).
34. Bin, M. *et al.* Coherent X-ray Scattering Reveals Nanoscale Fluctuations in Hydrated Proteins. *J. Phys. Chem. B* **127**, 4922–4930 (2023).
35. Reiser, M. *et al.* Resolving molecular diffusion and aggregation of antibody proteins with megahertz X-ray free-electron laser pulses. *Nat. Commun.* **13**, 5528 (2022).
36. Rodrigues, M. Q., Alves, P. M. & Roldão, A. Functionalizing Ferritin Nanoparticles for Vaccine Development. *Pharmaceutics* **13** (2021).
37. Wang, Z. *et al.* Ferritin nanocage-based antigen delivery nanoplatfoms: epitope engineering for peptide vaccine design. *Biomater. Sci.* **7**, 1794–1800 (2019).
38. Zhu, Y. *et al.* Ferritin-based nanomedicine for disease treatment. *Med. Rev.* **3**, 49–74 (2023).
39. He, D. & Marles-Wright, J. Ferritin family proteins and their use in bionanotechnology. *European Congress of Biotechnology - ECB 16* **32**, 651–657 (2015).
40. Uchida, M., Kang, S., Reichhardt, C., Harlen, K. & Douglas, T. The ferritin superfamily: Supramolecular templates for materials synthesis. *Biochim. Biophys. Acta - General Subjects* **1800**, 834–845 (2010).
41. Beenakker, C. & Mazur, P. Diffusion of spheres in a concentrated suspension: Resummation of many-body hydrodynamic interactions. *Phys. Lett. A* **98**, 22–24 (1983).
42. Beenakker, C. The effective viscosity of a concentrated suspension of spheres (and its relation to diffusion). *Physica A* **128**, 48–81 (1984).
43. Westermeier, F. *et al.* Structure and short-time dynamics in concentrated suspensions of charged colloids. *J. Chem. Phys.* **137**, 114504 (2012).
44. Madsen, A. *et al.* Materials Imaging and Dynamics (MID) instrument at the European X-ray Free-Electron Laser Facility. *J. Synchrotron Radiat.* **28**, 637–649 (2021).

45. Jian, N., Dowle, M., Horniblow, R. D., Tselepis, C. & Palmer, R. E. Morphology of the ferritin iron core by aberration corrected scanning transmission electron microscopy. *Nanotechnology* **27**, 46LT02 (2016).
46. Williams, G. & Watts, D. C. Non-symmetrical dielectric relaxation behaviour arising from a simple empirical decay function. *Trans. Faraday Soc.* **66**, 80–85 (1970).
47. Arbe, A. & Colmenero, J. Characterization of the “simple-liquid” state in a polymeric system: Coherent and incoherent scattering functions. *Phys. Rev. E* **80**, 041805 (2009).
48. De Gennes, P. G. Liquid dynamics and inelastic scattering of neutrons. *Physica* **25**, 825–839 (1959).
49. Nygård, K. *et al.* Anisotropic de Gennes Narrowing in Confined Fluids. *Phys. Rev. Lett.* **116**, 167801 (2016).
50. Braun, M. K. *et al.* Crowding-Controlled Cluster Size in Concentrated Aqueous Protein Solutions: Structure, Self- and Collective Diffusion. *J. Phys. Chem. Lett.* **8**, 2590–2596 (2017).
51. Holzweber, K., Tietz, C., Fritz, T. M., Sepiol, B. & Leitner, M. Beam-induced atomic motion in alkali borate glasses. *Phys. Rev. B* **100**, 214305 (2019).
52. Myint, P. *et al.* de Gennes Narrowing and Relationship between Structure and Dynamics in Self-Organized Ion-Beam Nanopatterning. *Phys. Rev. Lett.* **126**, 016101 (2021).
53. Wu, B., Iwashita, T. & Egami, T. Atomic Dynamics in Simple Liquid: de Gennes Narrowing Revisited. *Phys. Rev. Lett.* **120**, 135502 (2018).
54. Dallari, F. *et al.* Microsecond hydrodynamic interactions in dense colloidal dispersions probed at the European XFEL. *IUCr* **8** (2021).
55. Häussler, W. & Farago, B. Diffusive dynamics of ordered solutions of apoferritin near the structure factor peak. *J. Phys.:Cond. Matter* **15**, s197–s204 (2003).
56. Häussler, W. Structure and dynamics in Apoferritin solutions with paracrystalline order. *Chem. Phys.* **292**, 425–434 (2003).
57. Blaaderen, A. v., Peetermans, J., Maret, G. & Dhont, J. K. G. Long-time self-diffusion of spherical colloidal particles measured with fluorescence recovery after photobleaching. *J. Chem. Phys.* **96**, 4591–4603 (1992).
58. Genz, U. & Klein, R. Collective diffusion of charged spheres in the presence of hydrodynamic interaction. *Physica A* **171**, 26–42 (1991).
59. Harrison, P. M. The structure and function of ferritin. *Biochem. Educ.* **14**, 154–162 (1986).
60. Beenakker, C. Self-diffusion of spheres in a concentrated suspension. *Physica A* **120**, 388–410 (1983).
61. Petsev, D. N. *et al.* Temperature-independent solubility and interactions between apoferritin monomers and dimers in solution. *J. Cryst. Growth* **232**, 21–29 (2001).

62. Medina-Noyola, M. Long-Time Self-Diffusion in Concentrated Colloidal Dispersions. *Phys. Rev. Lett.* **60**, 2705–2708 (1988).
63. Hirschmann, F. *et al.* Effects of flexibility in coarse-grained models for bovine serum albumin and immunoglobulin G. *J. Chem. Phys.* **158**, 084112 (2023).
64. Szamel, G. & Leegwater, J. A. Long-time self-diffusion coefficients of suspensions. *Phys. Rev. A* **46**, 5012–5019 (1992).
65. Segrè, P. N. & Pusey, P. N. Scaling of the Dynamic Scattering Function of Concentrated Colloidal Suspensions. *Phys. Rev. Lett.* **77**, 771–774 (1996).
66. Holmqvist, P. & Nägele, G. Long-Time Dynamics of Concentrated Charge-Stabilized Colloids. *Phys. Rev. Lett.* **104**, 058301 (2010).
67. Banchio, A. J., Heinen, M., Holmqvist, P. & Nägele, G. Short- and long-time diffusion and dynamic scaling in suspensions of charged colloidal particles. *J. Chem. Phys.* **148**, 134902 (2018).
68. Leheny, R. L. XPCS: Nanoscale motion and rheology. *Curr. Opin. Colloid Interface Sci* **17**, 3–12 (2012).
69. Weeks, E. R., Crocker, J. C., Levitt, A. C., Schofield, A. & Weitz, D. A. Three-Dimensional Direct Imaging of Structural Relaxation Near the Colloidal Glass Transition. *Science* **287**, 627–631 (2000).
70. Mohanty, A., Parida, A., Raut, R. K. & Behera, R. K. Ferritin: A Promising Nanoreactor and Nanocarrier for Bionanotechnology. *ACS Bio. & Med. Chem. Au.* **2**, 258–281 (2022).
71. Grimaldo, M. *et al.* Protein Short-Time Diffusion in a Naturally Crowded Environment. *J. Phys. Chem. Lett.* **10**, 1709–1715 (2019).
72. May, M. E. & Fish, W. W. The uv and visible spectral properties of ferritin. *Arch. Biochem. Biophys.* **190**, 720–725 (1978).
73. Ghirlando, R., Mutskova, R. & Schwartz, C. Enrichment and characterization of ferritin for nanomaterial applications. *Nanotechnology* **27**, 045102 (2015).
74. Allahgholi, A. *et al.* The adaptive gain integrating pixel detector at the European XFEL. *J. Synchrotron Radiat.* **26**, 74–82 (2019).
75. Sztuk-Dambietz, J. *et al.* Operational experience with Adaptive Gain Integrating Pixel Detectors at European XFEL. *Front. Phys.* **11** (2024).
76. Falus, P., Lurio, L. & Mochrie, S. Optimizing the signal-to-noise ratio for X-ray photon correlation spectroscopy. *J. Synchrotron Radiat.* **13**, 253–259 (2006).

77. Cheng, N.-S. Formula for the Viscosity of a Glycerol-Water Mixture. *Ind. Eng. Chem. Res.* **47**, 3285–3288 (2008).
78. Ortega, A., Amorós, D. & García de la Torre, J. Prediction of Hydrodynamic and Other Solution Properties of Rigid Proteins from Atomic- and Residue-Level Models. *Biophys. J.* **101**, 892–898 (2011).
79. Mohanty, A., K, M., Jena, S. S. & Behera, R. K. Kinetics of Ferritin Self-Assembly by Laser Light Scattering: Impact of Subunit Concentration, pH, and Ionic Strength. *Biomacromolecules* **22**, 1389–1398 (2021).
80. Lehmkuhler, F. *et al.* Emergence of Anomalous Dynamics in Soft Matter Probed at the European XFEL. *Proc. Natl. Acad. Sci. U.S.A.* **117**, 24110–24116 (2020).
81. Biehl, R. Jscatter, a program for evaluation and analysis of experimental data. *PLoS One* **14**, e0218789 (2019).

# Supplementary Information:

## Coherent X-rays reveal anomalous molecular diffusion and cage effects in crowded protein solutions

Anita Girelli<sup>1,2,\*</sup>, Maddalena Bin<sup>1</sup>, Mariia Filianina<sup>1</sup>, Michelle Dargasz<sup>3</sup>, Nimmi Das Anthuparambil<sup>3</sup>, Johannes Möller<sup>4</sup>, Alexey Zozulya<sup>4</sup>, Iason Andronis<sup>1</sup>, Sonja Timmermann<sup>3</sup>, Sharon Berkowicz<sup>1</sup>, Sebastian Retzbach<sup>2</sup>, Mario Reiser<sup>1</sup>, Agha Mohammad Raza<sup>3</sup>, Marvin Kowalski<sup>3</sup>, Mohammad Sayed Akhundzadeh<sup>3</sup>, Jenny Schrage<sup>3</sup>, Chang Hee Woo<sup>10</sup>, Maximilian D. Senft<sup>2</sup>, Lara Franziska Reichart<sup>2</sup>, Aliaksandr Leonau<sup>3</sup>, Prince Prabhu Rajaiah<sup>5,6</sup>, William Chèvremont<sup>7</sup>, Tilo Seydel<sup>8</sup>, Jörg Hallmann<sup>4</sup>, Angel Rodriguez-Fernandez<sup>4</sup>, Jan-Etienne Pudell<sup>4</sup>, Felix Brausse<sup>4</sup>, Ulrike Boesenberg<sup>4</sup>, James Wrigley<sup>4</sup>, Mohamed Youssef<sup>4</sup>, Wei Lu<sup>4</sup>, Wonhyuk Jo<sup>4</sup>, Roman Shayduk<sup>4</sup>, Anders Madsen<sup>4</sup>, Felix Lehmkuhler<sup>5,9</sup>, Michael Paulus<sup>10</sup>, Fajun Zhang<sup>2</sup>, Frank Schreiber<sup>2</sup>, Christian Gutt<sup>3</sup>, and Fivos Perakis<sup>1,\*</sup>

<sup>1</sup>Department of Physics, AlbaNova University Center, Stockholm University, 10691 Stockholm, Sweden

<sup>2</sup>Institut für Angewandte Physik, Universität Tübingen, Auf der Morgenstelle 10, 72076 Tübingen, Germany

<sup>3</sup>Department Physik, Universität Siegen, Walter-Flex-Strasse 3, 57072 Siegen, Germany

<sup>4</sup>European X-Ray Free-Electron Laser Facility, Holzkoppel 4, 22869 Schenefeld, Germany

<sup>5</sup>The Hamburg Centre for Ultrafast Imaging, Luruper Chaussee 149, 22761 Hamburg, Germany

<sup>6</sup>Institute for Biochemistry and Molecular Biology, Laboratory for Structural Biology of Infection and Inflammation, University of Hamburg, c/o DESY, 22603, Hamburg, Germany

<sup>7</sup>ESRF - The European Synchrotron, 71 Avenue des Martyrs, 38042 Grenoble, France

<sup>8</sup>Institut Laue-Langevin, 71 Avenue des Martyrs, 38042 Grenoble, France

<sup>9</sup>Deutsches Elektronen-Synchrotron DESY, Notkestr. 85, 22607 Hamburg, Germany

<sup>10</sup>Fakultät Physik/DELTA, TU Dortmund, 44221 Dortmund, Germany

\*Email: anita.girelli@fysik.su.se, f.perakis@fysik.su.se

### Table of contents

<b>1</b>	<b>Data filtering</b>	<b>2</b>
<b>2</b>	<b>Structure factor interpolation</b>	<b>2</b>
<b>3</b>	<b>Assessment of beam-induced effects</b>	<b>3</b>
<b>4</b>	<b>Estimation of protein diffusion coefficient in the dilute limit</b>	<b>7</b>
<b>5</b>	<b><math>H(q)</math> model fit</b>	<b>7</b>

## 1 Data filtering

To achieve a sufficient signal-to-noise ratio (SNR), the measurements were repeated multiple times, including different sample positions, capillaries and batches of samples. Two filtering criteria were applied to ensure data quality, based on (1) the sample position and (2) the two-time correlation (TTC) functions. The first filter excluded measurements where the capillary was only partially hit or air bubbles were present. For the second filter we computed the average value and the standard deviation on a single train basis. The parameters chosen for the calculation of the correlation functions are shown in Table S1, including the protein concentration,  $c$ , number of pulses per train,  $n_{\text{pulses}}$ , number of repetitions,  $n_{\text{rep}}$ , incident X-ray transmission,  $T_0$ , and corresponding fluence.

**Table S1 | XPCS parameters for the calculation of the  $g_2(q, t)$**

$c$ (mg/ml)	$n_{\text{pulses}}$	$n_{\text{rep}}$	$T_0$	Fluence (nJ/ $\mu\text{m}^2$ /pulse)
70	120	5000	$5.35 \times 10^{-6}$	7.14
180	120	5000	$5.35 \times 10^{-6}$	7.19
400	120	5000	$5.35 \times 10^{-6}$	7.27
730	120	5000	$5.35 \times 10^{-6}$	7.41

## 2 Structure factor interpolation

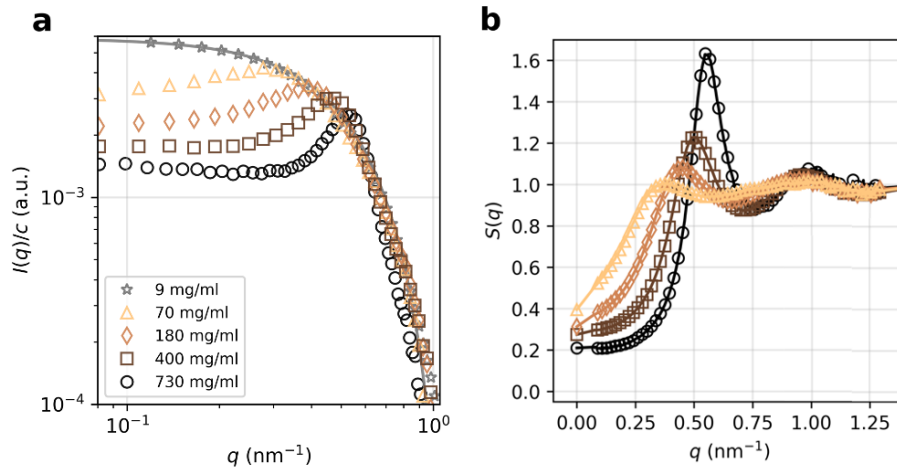


**Fig. S1 |** (a) Scattering intensity,  $I(q)$ , from the first pulse per train for various concentrations  $c$  and transmission value  $T_0 = 5.35 \times 10^{-6}$ . The solid line is a fit using the spherical form factor. (b) The experimental data of structure factor,  $S(q)$ , at various concentrations (as indicated by the symbols in the legend) and their interpolated values (solid lines).

In Fig. S1a is shown the scattering intensity,  $I(q)$ , as reported in the main manuscript, but in a log-log scale. The corresponding structure factor,  $S(q)$ , was determined by ensuring that its values at high  $q$  oscillated around 1. The validity of the normalization was checked by comparing the data with those obtained at ESRF (see main manuscript), which allowed for measurements at higher  $q$  values. The experimental  $S(q)$  data and their interpolated values used for the calculation of the  $\delta\gamma$  theory are shown in Fig.S1b. To ensure reliable results, we included the values  $S(\infty) = 1$  and  $S(0) = C_{\text{lin}}S(q_{\text{min}})$ , where  $C_{\text{lin}}$  is the intercept from a linear fit of the  $S(q)$  in a  $q$ -range between 0.07 and  $0.125 \text{ nm}^{-1}$ .

### 3 Assessment of beam-induced effects

Establishing optimal measurement conditions, where both structural and dynamic properties are not affected by the X-ray beam, is crucial for XPCS. Following approaches of previous studies [1], we monitored changes in both the scattering intensity,  $I(q)$ , and diffusion coefficient,  $D(q)$ .

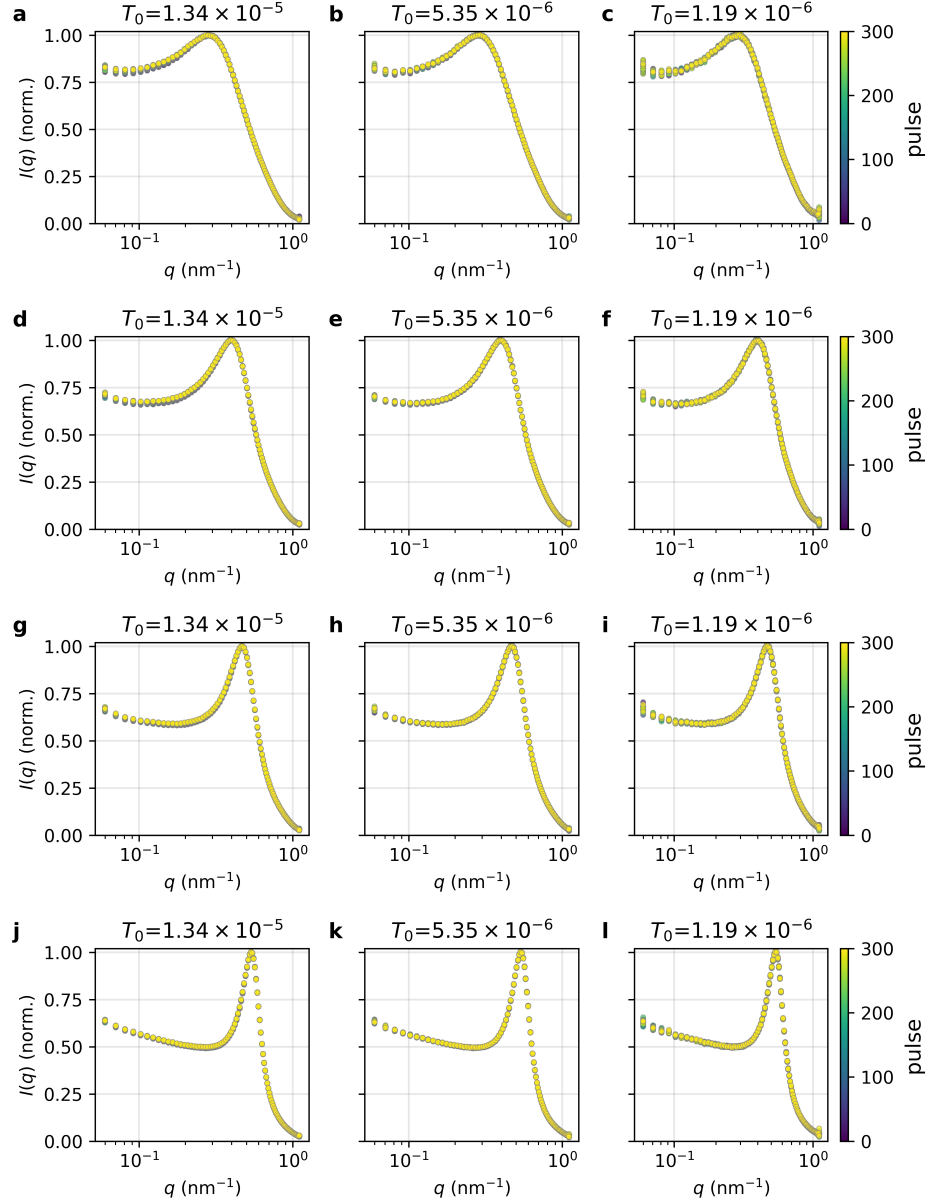


**Fig. S2** | Scattering intensity,  $I(q)$ , normalised by the intensity value at the peak position  $q_0$  at different transmission values  $T_0$ , and concentrations  $c = 70$  mg/ml (a-c),  $c = 180$  mg/ml (d-f),  $c = 400$  mg/ml (g-i) and  $c = 730$  mg/ml (j-l). The colors correspond to different pulse numbers as indicated in the color bar.

In Fig. S2, the  $I(q)$  at different transmission values,  $T_0$ , and concentrations,  $c$ , is shown. The only visible changes in the intensity involve a subtle increase in the small  $q$  region ( $q < 0.4 \text{ nm}^{-1}$ ). To quantify this change, we calculate the mean scattering intensity over  $0.1 \text{ nm}^{-1} < q < 0.3 \text{ nm}^{-1}$ , normalised to the intensity value of the first pulse, which is shown in Fig.S3. A linear increase of the signal as a function of train pulse number,  $n_{pulse}$ , was observed for all concentrations  $c$  and transmission values  $T_0$ . Under the measurements conditions presented in the main paper ( $n_{pulse} = 120$ ,  $T_0 = 5.35 \times 10^{-6}$ ), the relative changes were less than 0.5%.

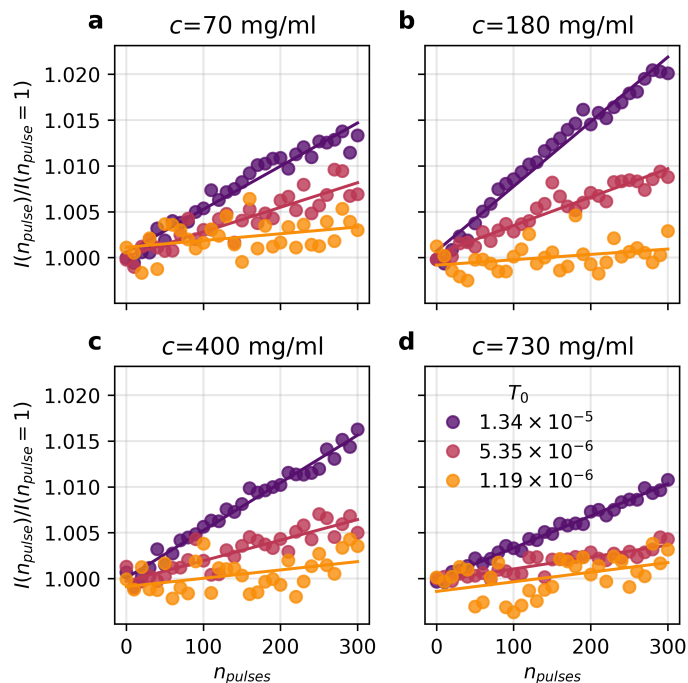


**Fig. S3** | The scattering intensity,  $I(q)$ , averaged over the range  $0.1 \text{ nm}^{-1} < q < 0.3 \text{ nm}^{-1}$ , normalised by the scattering intensity at the first pulse,  $I(n_{pulse} = 1)$ , as a function of pulse number  $n_{pulse}$  for the various transmission values,  $T_0$ , and concentrations,  $c$ .

From the TTC maps shown in Fig.S4, it is possible to quantify possible beam-induced effects on dynamics. The data reveal no noticeable changes in the width along the diagonal. This observation, combined with the changes below 0.5% seen in the  $I(q)$ , suggests that protein aggregation is not detected within the timescale probed.

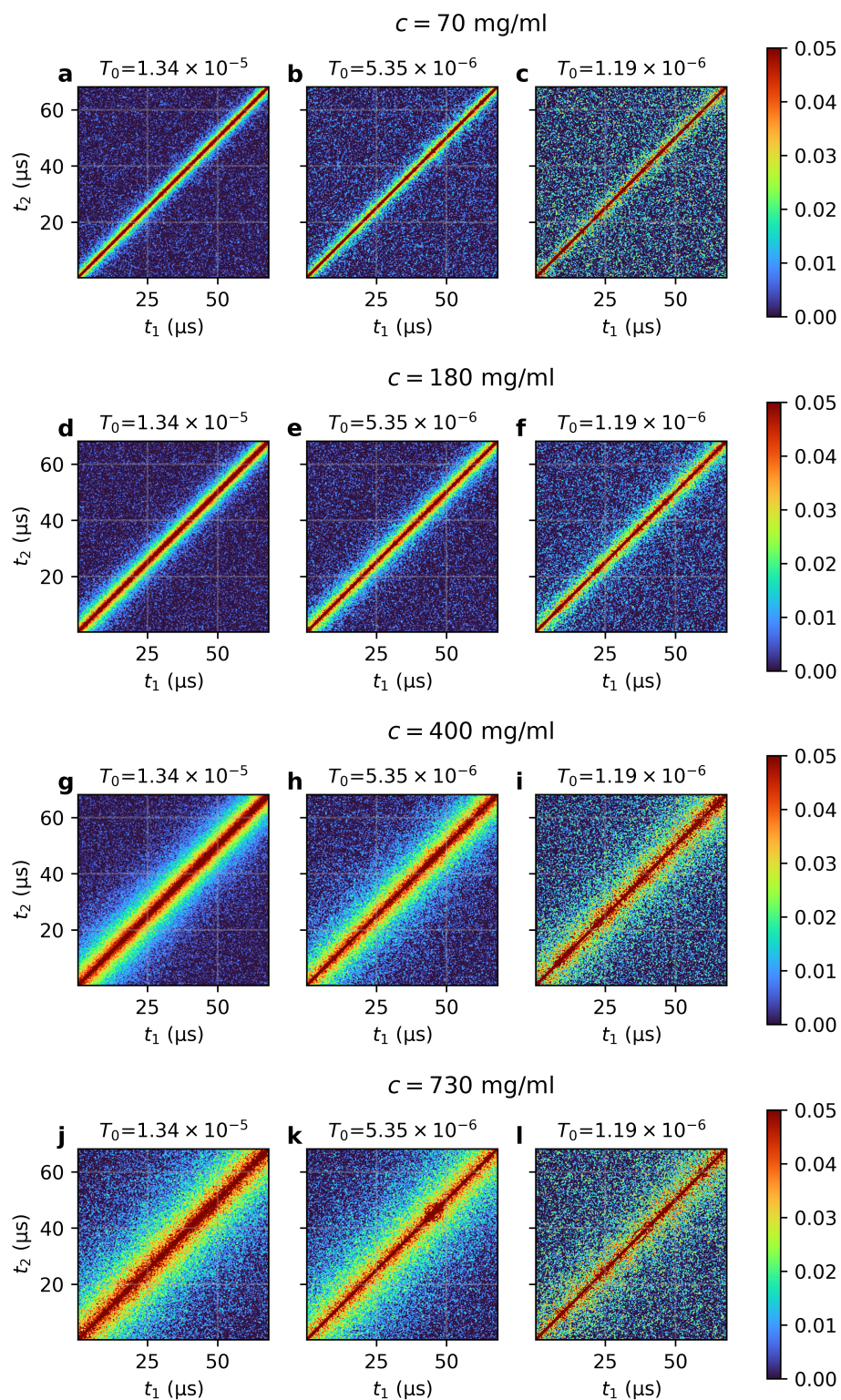


**Fig. S4** | TTCs at  $0.275 \text{ nm}^{-1} < q < 0.325 \text{ nm}^{-1}$  measured at 25 C for a protein concentration of (a-c) 70 mg/ml, (d-f) 180 mg/ml, (g-i) 400 mg/ml, (j-l) 730 mg/ml, with different beam transmissions reported on the top of each panel.

More subtle X-ray beam-induced effects can be quantified by examining the changes of the intensity autocorrelation function  $g_2$  line shape. To compute the  $g_2$  functions, 100 pulses were used and the initial and final pulse were varied to track possible changes in the diffusion as function of pulse number. Each  $g_2$  curve was associated with a pulse number, which is the average of the first and the last pulse numbers. The correlation functions were fitted with a stretched exponential function, as in the main manuscript. Figure S5a shows the resulting diffusion coefficients, averaged over  $0.275 \text{ nm}^{-1} < q < 0.375 \text{ nm}^{-1}$ , as a function of pulse number. We attribute the observed changes to beam-induced heating [1, 2]. The temperature increase is quantified by the rise in the value of the diffusion coefficient using Stokes-Einstein equation,  $D(T + \Delta T) = k_b(T + \Delta T)/[6\pi\eta(T + \Delta T)R]$ , by accounting for the increase in diffusion coefficient and change in viscosity. The estimated temperature rise is shown in Table S2. The corresponding Kohlrausch-Williams-Watts (KWW) exponent,  $\alpha$ , is shown in Fig S5b, where  $\alpha$  remains nearly constant as a function of pulse number.

**Table S2** | Beam-induced temperature increase estimated for the parameters used for the calculation of the correlation functions shown in Fig.3 (in the main paper). The parameters used are  $T_0 = 5.35 \times 10^{-6}$  and  $n_{pulses} = 120$ .

$c$ (mg/ml)	$\Delta T$ (K)
70	$0.95 \pm 0.11$
180	$0.65 \pm 0.09$
400	$1.07 \pm 0.07$
730	$0.85 \pm 0.11$

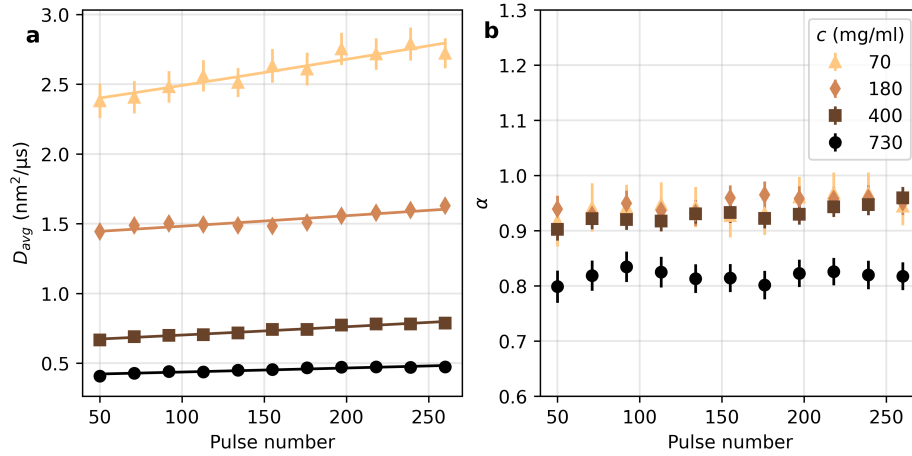


**Fig. S5** | (a) The diffusion coefficient, averaged over  $0.275 \text{ nm}^{-1} < q < 0.375 \text{ nm}^{-1}$ , as a function of pulse number for different concentrations. The solid line represent the fitted increase of diffusion coefficient due to temperature increase. (b) The Kohlrausch-Williams-Watts (KWW) exponent,  $\alpha$ , as a function of pulse number for different concentrations.

## 4 Estimation of protein diffusion coefficient in the dilute limit

The protein diffusion coefficient,  $D_0$ , in the dilute limit and the corresponding hydrodynamic radius  $R_h$  were estimated with DLS by measuring a solution with  $c = 9$  mg/ml in water-glycerol (55 vol% glycerol). The measurement was performed with a LS spectrometer (LS Instruments AG) equipped with a  $\lambda = 660$  nm CW laser. The computed  $g_2$  functions are reported in Fig.S6a. The decorrelation rate  $\Gamma(q)$  was extracted by fitting a single exponential decay, with the expression  $g_2(q, t) = \beta(q) \exp[-2t\Gamma(q)]$ . The extracted decorrelation rates are shown in Fig. S6b.

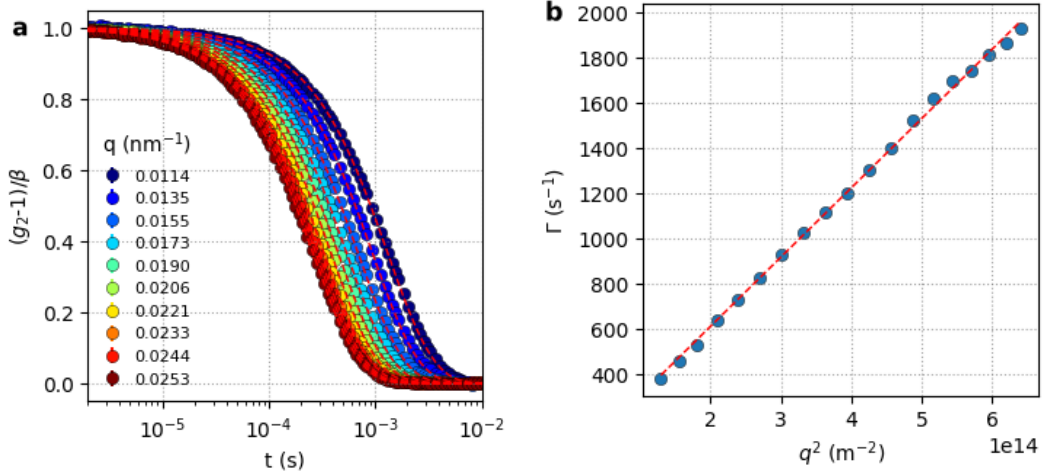


**Fig. S6 | Dynamic light scattering (DLS) measurements of ferritin solutions.** The data shown correspond to dilute condition ( $c = 9$  mg/ml) in water-glycerol (with glycerol volume fraction  $\nu_{\text{glyc}} = 0.55$ ) (a) The intensity autocorrelation functions,  $g_2(q, t)$ , is shown for different  $q$  values, as indicated in the legend. The  $g_2(q, t)$  is normalised by the corresponding speckle contrast,  $\beta$ . (b) The extracted decorrelation rate,  $\Gamma(q)$ , obtained from the  $g_2(q, t)$  using a single exponential fit. The solid line is a linear fit and the slope gives the diffusion coefficient  $D_0$  in the dilute limit.

## 5 $H(q)$ model fit

To fit the experimental  $H(q)$  data, the model was scaled with a concentration-dependent factor. This factor is present due to the influence of direct protein interactions on the diffusion. In more detail, since for this system  $D^{\text{long}}(q)$  and  $D^{\text{short}}(q)$  have the same  $q$ -dependence, we can combine Eq. 2 and Eq. 5 of the main paper so that:

$$D^{\text{long}}(q) = \frac{D^{\text{short}}(q)}{D_0} \cdot D_s^{\text{direct}} = \frac{H(q)}{S(q)} D_s^{\text{direct}} \quad (\text{S1})$$

Therefore, for the  $H(q)$  model to be able to describe the long-time diffusion an additional factor has to be taken into account. To verify the validity of Eq. S1, we compare the experimental  $D^{\text{long}}(q)/D^{\text{short}} = D_2(q)/D_1(q) = 0.12 \pm 0.04$  obtained from the two exponential fit for concentration 730 mg/ml with the expected value of  $D_s^{\text{direct}}/D_0 = 1/(1 + 2\chi\phi_h) = 0.13$ , which shows good agreement.

At low protein concentration ( $c = 70$  mg/ml) the correlation functions  $g_2$  show Brownian motion ( $\alpha \approx 1$ ) suggesting that the short-time diffusion is the main contribution on the observed dynamics. At intermediate protein concentrations ( $c = 180$ -400 mg/ml), anomalous diffusion is evident with  $\alpha < 1$ ,

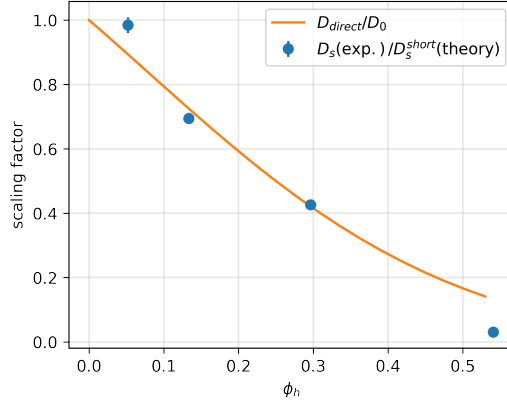


**Fig. S7** | The scaling factor (blue circles) relates to the ratio of the experimental  $D_s$  over the theoretical short-time self-diffusion coefficient. The orange solid line represents the value of  $D_s^{\text{direct}}/D_0 = 1/(1 + 2\chi\phi_h)$  where  $\chi$  the contact value of the pair-correlation function was estimated approximating the protein interactions as hard spheres ( $\chi = (1 + 0.5\phi)/(1 - \phi)^2$ ).

due to contributions from both short- and long-time diffusion. As a consequence, the resulting diffusion coefficient and hydrodynamic functions shown in Figs. 3 and 4 (main paper) contain contributions from both short- and long-time diffusion. Since the value of  $D_s/D_0$  for these concentrations seem to follow more closely the long-time diffusion equation, we assume that the contribution of the long-time diffusion is dominating the signal. To understand the contribution of the long-time diffusion in the signal at the various protein concentrations measured, we compare the scaling factor, hence the ratio of the experimental  $D_s$  over the theoretical value of  $D_s^{\text{short}}$  (Eq.15 of the main paper) and compare it with the theoretical value of  $D_s^{\text{direct}}/D_0$ . Figure S7 shows that for the lowest concentration (70 mg/ml) no correction factor is needed, consistent with the notion that we are probing only the short-time diffusion. For the intermediate concentrations ( $c = 180\text{-}400$  mg/ml), the values are consistent with the model. For the highest concentrations (730 mg/ml), there is a deviation, possibly because the model of  $D_s^{\text{short}}$  is valid only for volume fractions up to  $\phi = 0.45$  according to Ref.[3].

## References

1. Reiser, M. *et al.* Resolving molecular diffusion and aggregation of antibody proteins with megahertz X-ray free-electron laser pulses. *Nat. Commun.* **13**, 5528 (2022).
2. Lehmkuhler, F. *et al.* Emergence of Anomalous Dynamics in Soft Matter Probed at the European XFEL. *Proc. Natl. Acad. Sci. U.S.A.* **117**, 24110–24116 (2020).
3. Beenakker, C. Self-diffusion of spheres in a concentrated suspension. *Physica A* **120**, 388–410 (1983).